Spring 2019

An Anatomical Basis of the Differential Cholinergic Modulation of Valence-Specific Pyramidal Neurons in the Basolateral Amygdala

Nguyen Vu

An Anatomical Basis of the Differential Cholinergic Modulation of Valence-Specific Pyramidal Neurons in the Basolateral Amygdala

by

Nguyen Vu

Bachelor of Science
University of South Carolina, 2016

Submitted in Partial Fulfillment of the Requirements

For the Degree of Master of Science in

Biomedical Science

School of Medicine

University of South Carolina

2019

Accepted by:

David D. Mott, Director of Thesis

Robert Price, Reader

Alexander J. McDonald, Reader

Jay Potts, Reader

Cheryl L. Addy, Vice Provost and Dean of the Graduate School

ACKNOWLEDGEMENTS

I would like to thank my mentors for all your guidance and support, and for spending time teaching me from the basics, from science to life lessons

…to Dr. James Warren for all the injections in this study

… to the friends I've made at SOM, especially the Mott's lab crew and everyone in IRF, for making my time here much more enjoyable

… and to all my friends and family, especially my parents and sister for your unconditioned love and support. You are the reason for me to keep going.

ABSTRACT

Emotion is a crucial component of the decision-making process. The amygdala, known as the “orchestrator” of the emotion circuit, associates emotional valence with incoming sensory stimuli and thus contributes to decision-making. Within the basolateral nucleus of the amygdala (BLA), spatially segregated and genetically distinct pyramidal neurons (PNs) have been identified based on their correspondence to distinct behavioral stimuli. These PNs project to several brain regions mediating different aspects of the emotional spectrum. For example, BLA PNs projecting to prelimbic (PL) and infralimbic (IL) cortex are involved in fear acquisition and fear extinction, respectively. However, the mechanism by which these distinct PNs are modulated and whether this modulation differs depending on their projection targets remains unclear. The BLA is densely innervated by cholinergic fibers from the basal forebrain, and the contributions of acetylcholine (ACh) to selective attention, emotion, and other cognitive functions suggest a modulatory role of this neurotransmitter in the BLA. Here, we have used confocal immunofluorescence to examine the anatomical distribution of cholinergic markers across the BLA relative to PNs, including those projecting to PL and IL, to establish an anatomical basis for cholinergic modulation of different PNs. Immunoreactivity for both postsynaptic M1 muscarinic receptors and vesicular ACh transporter (vAChT), a marker of cholinergic terminals, was significantly greater in the dorsorostral region of the

anterior BLA (BLAa) compared to other regions of the BLA or other amygdalar subnuclei (n=6). M1R immunoreactivity was preferentially localized to magnocellular PNs in the BLAa (n = 6). These magnocellular PNs have previously been found to be responsive to stimuli of negative valence. In contrast, parvocellular PNs, which are responsive to stimuli of positive valence, were located in posterior BLA (BLAp), exhibited significantly less M1R immunoreactivity and were associated with significantly less cholinergic innervation. PNs projecting to PL (PL-projectors), which were prominently found in BLAa, expressed higher M1 intensity than those projecting to IL, which were more equally distributed between BLA subnuclei. Altogether, these data provide an anatomical basis for preferential cholinergic modulation of negative valence-encoding PNs in the BLA.

TABLE OF CONTENTS

LIST OF FIGURES

LIST OF ABBREVIATIONS

ACh ..... Acetylcholine

AP ..... Anteroposterior

BF ..... Basal forebrain

BL ..... Basolateral amygdaloid complex

BLA ..... Basolateral amygdalar nucleus

BLAa ..... Basolateral amygdala, anterior subdivision

BLAp ..... Basolateral amygdala, posterior subdivision

BMA ..... Basomedial amygdala

BMAp ..... Basomedial amygdala, posterior subdivision

BLAv ..... Basolateral amygdala, ventral subdivision

CeA ..... Central amygdalar nucleus

CeAc ..... Central amygdalar nucleus, capsular part

CeAm ..... Central amygdalar nucleus, medial part

CeAl ..... Central amygdalar nucleus, lateral part

CNS ..... Central nervous system

CtB 555 ..... Cholera toxin subunit B, conjugated with Alexa Fluor 555

CtB 647 ..... Cholera toxin subunit B, conjugated with Alexa Fluor 647

DV ..... Dorsoventral

IGT ..... Iowa gambling task

IL ..... Infralimbic cortex

LA ..... Lateral amygdalar nucleus

LaVL ..... Lateral amygdala, ventrolateral subdivision

M1R ..... M1 subtype of the muscarinic acetylcholine receptor

mAChR ..... Muscarinic acetylcholine receptor

NAc ..... nucleus accumbens

nAChR ..... nicotinic acetylcholine receptor

NDS ..... Normal donkey serum

NGS ..... Normal goat serum

PB ..... Phosphate buffer solution

PBS ..... Phosphate-buffered saline solution

PD ..... Parkinson's disease

PFA ..... Paraformaldehyde

PL ..... Prelimbic cortex

PN ..... Pyramidal neurons

Ppp1r1b ..... Protein phosphatase 1 regulatory inhibitor subunit 1B

PTSD ..... Posttraumatic stress disorder

ROI ..... Region of interest

Rspo2 ..... R-spondin2

SCR ..... Skin conductance responses

TB ..... Tris-buffered solution

TBS ..... Tris-buffered saline solution

vAChT ..... Vesicular acetylcholine transporter

VMPC ..... Ventromedial prefrontal cortex

CHAPTER I: INTRODUCTION

A) **Emotion and Decision-Making**:

People make decisions every day. In his book *The Paradox of Choice: Why more is less*, psychologist Barry Schwartz discussed the unfathomable amount of choices that an average American has to face (Schwartz). We make decisions from the moment we wake up until we go to bed at night. It seems that we as a society are being impacted by facets of choices. Most people are probably not able to remember the majority of the normal, mundane choices they make every day. However, many can recall precisely the more impactful decisions made during critical situations, such as swerving left or right during a car accident. During those moments, people make seemingly instantaneous decisions that they can almost always recall vividly and accurately later. Notably, people experience a strong rush of emotions, such as nervous, shocked, surprised, etc., which is often lacking when making ordinary choices. Not only do people remember emotional experiences better, those very emotions can subsequently alter the decisions that they make, either rationally or irrationally. In a 2016 study, subjects participating in tasks that engaged positive emotions showed less tendency in retrieving prior experiences and memories; and in general made overconfident judgements (Treffers and Fehse 2016). It may not seem as obvious but the so-called mundane choices we make every day are also emotionally driven. People tend to stick to choices that have given them positive

experiences in the past and avoid selecting risky choices associated with negative memory. Therefore, emotion is considered as a crucial component of the intricate network of decision-making.

As discussed above, most of the decisions we make are guided by emotion, either consciously or unconsciously. In his recent work, *The Disordered Mind*, neuroscientist Eric Kandel used a simple model to describe emotions with two axes that represent valence and intensity (Kandel 2018: 179). Valence is the value of emotion that determines behavioral outcomes and intensity is the strength of the emotion. This simplistic model is adequate to portray the complexity of emotion as a continuous spectrum. As people make decisions, contextual and environmental stimuli are perceived and interpreted. Stimuli are often categorized as either positive or negative, which can induce positive or negative reinforcements. The ability to precisely differentiate and evaluate different stimuli for appropriate responses is crucial and often seems trivial for healthy individuals. However, those with affective disorders, such as post-traumatic stress disorder (PTSD) or anxiety disorders, find it immensely difficult to match their emotions to various stimuli from their surroundings. A fMRI study on psychopathic inmates showed a correlation between their deficient paralimbic system, including many structures responsible for emotional processing, and their impaired moral judgements (Kiehl and Hoffman 2011). Specifically, investigators detected increased activation in the amygdala, a structure in the limbic system responsible for assigning emotional values to sensory stimuli, of psychopathic inmates compared to non-psychopathic inmates during moral

reasoning tasks. Interestingly, these psychopaths showed greatly reduced activity in the amygdala but increased activity in the lateral frontal cortex, a region involved in cognitive functions, during an affective memory task (Kiehl and Hoffman 2011). A typical relationship between stimulus and valence would be how positive input elicits appetitive or approaching behavior, whereas negative input induces aversive or avoidance behavior. For example, an animal would normally approach a positive stimulus such as food but avoid a negative stimulus such as a predator. However, depending on the contextual cues or other convergent stimuli, this basic relationship may differ. For instance, the animal would choose to suppress its fear towards its imminent threat and would risk its life in protecting its offspring from predators. As we discussed earlier, these decisions are often made instantaneously. However, the exact mechanism through which individuals precisely distinguish and evaluate opposing stimuli during emotional decision-making remains elusive.

This study investigated the anatomical framework of the modulatory mechanism of opposing valences in response to various stimuli as part of the emotional decision-making circuitry. By understanding this mechanism better, we can offer further insight into differences in the regulatory models between normal and disordered minds, especially mood disorders with decision-making deficits.

B) The Role of The Amygdala in Emotional Decision-Making:

Decision-making deficits have been reported in individuals who have suffered from neuropsychiatric disorders such as addiction, pathological gambling, Parkinson's disease (PD), etc. (Bechara 2001; Kobayakawa et al.

2010). Previous studies on decision-making have been using the Iowa Gambling Task (IGT) as a standard tool to assess participants' abilities in making choices. The major requirements in IGT that ensure its assimilation to real-life decision-making are the uncertainty of outcomes and the variability in rewards and punishments (Gupta et al. 2011).Participants choose multiple cards, one by one, from four decks of cards. Each selection comes with monetary rewards and punishments. The four decks are split into advantageous and disadvantageous decks. By using this tool, several studies indicated that multiple neural structures are involved in different aspects of decision-making, particularly the ventromedial prefrontal cortex (VMPC) and the amygdala (Bechara et al. 1994; Bechara et al. 1999; Bechara et al. 2000; Bechara et al. 2003). Compared to control subjects, patients with bilateral amygdalae damages as well as those with bilateral VMPC damages preferred the disadvantageous decks (immediate, large rewards but delayed, larger punishments), which eventually yield an overall loss (Bechara et al. 1999; Bechara et al. 2003). Similar results were also observed in substance abusers, pathological gamblers, PD patients, bipolar disorder patients, etc. (Bechara and Damasio 2002; Kobayakawa et al. 2008; Yechiam et al. 2008; Kobayakawa et al. 2010). Participants with dysfunctional amygdalae also showed a void in skin conductance responses (SCRs), a measure of reactivity of emotion that is normally generated in healthy individuals before and after picking a deck. In other words, these individuals fail to showcase the ability to integrate distinct emotional responses to opposing valences (the emotional aspects associated with winning and losing). Another example of the involvement of the amygdala in

decision-making is demonstrated in Parkinson's disease. PD patients also perform poorly on IGT tests with a preferential bias towards disadvantageous or risky selections (Kobayakawa et al. 2008; Kobayakawa et al. 2010). Kobayakawa and colleagues postulated that the tendency towards risky choices by PD patients is the consequence of emotional impairment from amygdala damage (Kobayakawa et al. 2010). Diminished emotional responses to both reward and punishment in PD patients were illustrated by lower SCRs and impaired recognition of facial expression of certain emotions (Kan et al. 2002; Sprengelmeyer et al. 2003; Suzuki et al. 2006; Kobayakawa et al. 2008). Emotional apathy associated with a dysfunctional limbic system involving the amygdala has also been observed in PD (Braak et al. 1994; Braak et al. 1996; Harding et al. 2002; Saito et al. 2003).

The amygdala, also referred to as the amygdaloid complex, is an almond-shaped structure that is morphologically and functionally organized into roughly 13 nuclei; of which the basolateral portion of the amygdala (BL) contains the largest cells of the complex (Krettek and Price 1978; Sah et al. 2003). The amygdala is considered as the "orchestrator" of emotion. The crucial role of the amygdala, specifically the BL, in orchestrating different emotional states by bridging the unconscious and conscious aspects of emotion is in large part due to its dense internuclear and intranuclear connections (Sah et al. 2003). To put it simply, as the BL receives sensory information from all modalities, it decodes and assigns emotional significance to those inputs. From there, it relays the decoded signals onward to different structures responsible for the conscious and

unconscious aspects of emotion. The unconscious route refers to the autonomic responses such as increasing heart rate, sweating, jumping, etc.; while the conscious part refers to the “feeling state” or essentially, the emotional state (Sah et al. 2003; Kandel 2018). According to the James-Lange theory of emotion, our bodily physiological response is the driving force of the conscious or emotional state (James 1884). Therefore, we feel because we react; or we’re scared because we run. The BL is comprised of the lateral (LA), basolateral (BLA), and the basomedial (BMA) nuclei (Krettek and Price 1978). The LA receives the majority of the sensory inputs to the amygdala (McDonald 1998; LeDoux 2003). Classical fear conditioning studies have demonstrated that the auditory conditioned stimuli (CS) that can induce fear response travel from the auditory thalamus directly to the amygdala and indirectly via the auditory cortex first before reaching the LA (Mascagni et al. 1993; Romanski and LeDoux 1993; McDonald 1998; LeDoux 2003). The direct thalamo-amygdala pathway is relatively quicker but not as precise as the indirect thalamo-cortico-amygdala pathway (Kandel 2018: 183). This explains why people react to loud noise instantly before registering the source of the noise. Morphologically, three neuronal classes have been identified in the LA and BLA: the predominant Class I of large, spiny, and pyramidal shaped neurons; Class II neurons, comprises ~5% of recorded neurons, are spine-sparse with smaller, ovoid cell bodies; several small, spherical neurons were classified as Class III (McDonald 1982).Class I neurons, also known as pyramidal or projection neurons (PNs), are further segregated into the anterior and posterior subdivisions of BLA based on

their perikaryal size. Magnocellular PNs, with relatively larger cell bodies, predominate the anterior portion of the BLA (BLAa) and parvocellular PNs, with relatively smaller cell bodies, populate the posterior portion (BLAp) (Krettek and Price 1978; McDonald 1982; Sah et al. 2003). Similarly, LA is also divided into larger-celled dorsolateral, smaller-celled ventrolateral, and intermediate subdivisions (Sah et al. 2003).

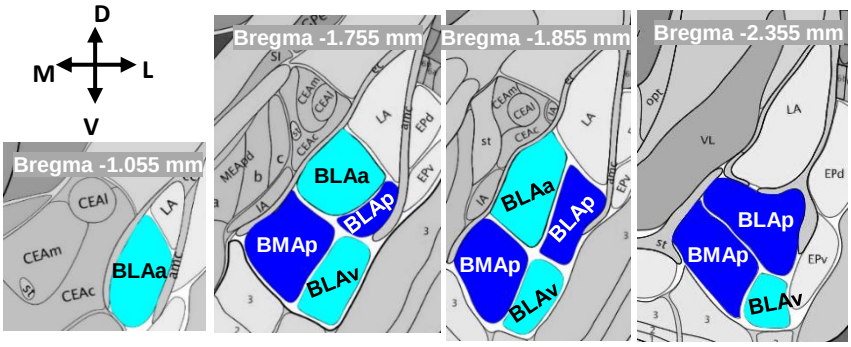

Figure 1.1 Color-coded Maps of the Distribution of Parvo- and Magno-cellular PNs in BLA. Magnocellular PNs (cyan) and parvocellular PNs (blue) from anterior to posterior BLA. Images of coronal sections obtained from the Allen Mouse Brain Atlas (2004). Available from: https://mouse.brain-map.org/static/atlas

Since amygdalae involvement in both appetitive and aversive behaviors has been established, recent studies have focused on investigating the determining factors that distinguish PNs in the BLA that are driving opposing valences (such as reward versus avoidance behaviors) (Namburi et al. 2015; Beyeler et al. 2016; Correia and Goosens 2016; Kim et al. 2016; Beyeler et al. 2018). One group suggested that the specificity of the valence encoded by BLA PNs is determined by their projection targets (Namburi et al. 2015; Beyeler et al. 2016; Beyeler et al. 2018). They reported that BLA PNs projecting to the nucleus

accumbens (NAc) and central amygdala (CeA) show, respectively, preferential responses to reward and aversion predictive cues (Beyeler et al. 2016). Topographically, they could not detect a gradient of neurons responsive to positive versus negative cues across the AP axis of the BLA. However, they were able to record a preferential coding bias along the DV axis with stronger responses to the positive cues recorded from BLA compared to LA (Beyeler et al. 2018). Another group, however, found that an anatomical and genetic segregation between BLA PNs corresponded to positive and negative valences (positive and negative neurons) (Kim et al. 2016). They identified two distinct genetic markers, Rspo2 (R-spondin2) and Ppp1r1b (protein phosphatase 1 regulatory inhibitor subunit 1B), exclusively expressed on negative and positive neurons, respectively. These genetically distinct and valence-specific neurons are also spatially segregated with an AP gradient across the BLA. Rspo2+ neurons overlap with magnocellular PNs in the BLAa while Ppp1r1b+ neurons correspond to parvocellular PNs in the BLAp. Interestingly, a recent study identified a neural ensemble within the amygdala that encodes the unpleasantness of pain and found these nociceptive neurons expressed the negative valence marker Rspo2 but not the positive valence marker Ppp1r1b (Corder et al. 2019).

C) Cholinergic Signaling in The Amygdala:

Since there is a dense cholinergic presence in the amygdala, it is of interest to study the role of this neuromodulator in modulating the opposing valence-encoding PNs in the BLA. Acetylcholine (ACh) is well-known in the

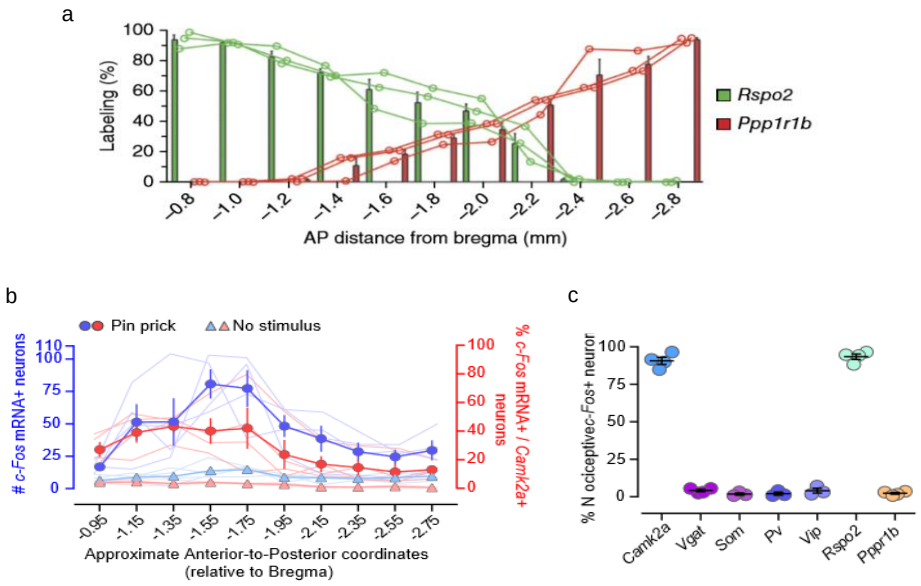

Figure 1.2 Graphs from Previous Reports on the Distribution of Valence-specific PNs in BLA. *a*: AP distribution of Rspo2+ and Ppp1r1b+ PNs (Kim et al., 2018). ***b, c***: Graphs from Corder et al., 2019 showing the distribution of nociceptive neurons from anterior to posterior BLA (c) with majority of them are PNs (Camk2a+) and express negative valence marker (Rspo2+) (d)

peripheral system as a primary excitatory neurotransmitter. However, its functional role in the central nervous system (CNS) is more complex. Unlike its counterpart in the periphery, central ACh is well-established as a neuromodulator. Some of its modulatory effects include alternating neuronal excitability, mediating neurotransmitter release, determining the fate of certain neuronal ensembles, etc. (Wonnacott 1997; Rice and Cragg 2004; Zhang and Sulzer 2004; Kawai et al. 2007). The cholinergic system contributes to the regulation of cognitive tasks such as attention, learning, and memory consolidation (Gold 2003; Power et al. 2003; Robinson et al. 2011). In fact, studies have shown correlation between cognitive impairment and cholinergic

system deficits. For instance, cholinergic cell loss is reported in Alzheimer's disease (Whitehouse et al. 1982; McGeer et al. 1984). Deficient ACh synthesis and a dysfunctional cholinergic system in aged and demented CNS were reported (Bartus et al. 1982). Similar cognitive dysfunctions were also observed in young subjects when their cholinergic systems were artificially disturbed (Bartus and Johnson 1976). Picciotto and colleagues reported in their 2012 review that the differential effects of cholinergic signaling on opposing behavioral responses are modulated by receptor subtypes, their density, the population of target, and the brain regions (Picciotto et al. 2012). BLA is densely innervated by cholinergic fibers from the basal forebrain with PNs as the major target of cholinergic innervation in BLA (Muller et al. 2011). Cholinergic signaling in BLA is essential for emotion-related cognitive tasks such as fear learning and consolidation of emotional memory (McGaugh 2004). Therefore, in order to elucidate the modulatory effect of ACh on the opposing stimuli-driven BLA PNs, it is imperative to look at the distribution pattern of cholinergic receptors relative to the positive-negative neurons.

The mechanism of ACh release is mediated by two classes of cholinergic receptors: the metabotropic muscarinic receptors (mAChRs) and the ionotropic nicotinic receptors (nAChRs). A 1982 review by Bartus and colleagues summarized results from previous studies on rodents and humans indicate an age-related reduction in muscarinic receptor density (Bartus et al. 1982). Similarly, a decrease in muscarinic receptors was reported in schizophrenic patients in several post-mortem studies (Crook et al. 2000; Dean et al. 2002;

Scarr et al. 2007). The mAChRs, belonged to the G-protein-coupled family, are further categorized into 5 different subtypes: Gq (M1, M3, M5), and Gi (M2, M4). Buckley et al. (1988) employed in situ hybridization techniques to investigate the distribution of m1-m4 mRNAs across the rat CNS. They demonstrated that m1 receptor (M1R) mRNAs predominate the BLA compared to other subtypes (Buckley et al. 1988). To compensate for the differences in mRNA's translation efficiency, other studies also looked at the protein expression of M1Rs and found similar results (Levey et al. 1991; McDonald and Mascagni 2010). Specifically, in the same study from 2010, McDonald and Mascagni further investigated the neuronal localization of M1Rs and found majority of M1 immunoreactivity in the cell bodies and proximal dendrite of BLA PNs. They also discovered an anatomical distribution of M1 across BLA and LA. The anterior subdivisions of both BLA and LA expressed the most "robust" M1 labeling (McDonald and Mascagni 2010). Altogether, these studies suggest an anatomical distribution of M1Rs across the BLA. This study offers further insight into this distribution in relation to BLA PNs that encode positive and negative valences.

D) Objective, Hypothesis, and Aims:

The objective of this study was to investigate the differential expression of M1 mAChR and vesicular ACh transporter (vAChT), a marker for cholinergic terminals, between magnocellular and parvocellular BLA PNs as well as between PL- and IL- projectors. These results can help portray an anatomical framework of the cholinergic modulation of BLA PNs that drive opposing behavioral

responses and to determine whether there is a preferential bias of this modulation based on their projection targets. Based on the 2010 report by McDonald and Mascagni on a topographical difference of M1R along the AP axis, we hypothesize that magnocellular and parvocellular PNs that are distinctly associated to anterior and posterior subdivisions of BLA also express a robust difference on M1R. We also hypothesize that PL projectors, which were prominently found in BLAa, express higher M1 intensity than IL projectors, which were more equally distributed between BLA subnuclei. To test these hypotheses, the following aims were proposed and accomplished:

Aim 1: Determine the differential expression of vAChT intensity across different BLA subnuclei.

Aim 2: Determine the differential expression of M1Rs intensity across different BLA subnuclei.

Aim 3: Determine the differential expression of M1Rs intensity between PL- and IL- projectors.

CHAPTER II: EXPERIMENTAL PROCEDURES

A) Tissue preparation and immunohistochemistry:

All animal handling and surgical procedures were conducted in accordance with the National Institutes of Health Guide for the Care and Use of Laboratory Animals and were approved by the Institutional Animal Use and Care Committee (IACUC) of the University of South Carolina. Three male and three female C57BL/6J mice (8-12 weeks, Jackson Laboratory, Bar Harbor, ME) were anesthetized with isoflurane and intracardially perfused with ice-cold 0.1M phosphate buffered saline (PBS, pH 7.4) containing 0.5% sodium nitrite followed by ice-cold 4% paraformaldehyde (PFA) in 0.4M phosphate buffer (PB, pH 7.4). Brains were immediately extracted and postfixed overnight in 4% PFA in PB (0.4M, pH7.4) at 4^{o}C. 50 µm thick horizontal sections were collected using a Vibratome (Leica Microsystems). Sections were stored in 0.1M PBS (pH 7.4) at 4^{o}C until further processing. Three sections from each animal were later obtained for vAChT labeling and 3 adjacent sections were used for M1R labeling. Horizontal sections labeled and imaged were divided across the dorsoventral (DV) axis of the BLA with the approximate Bregma as -4.44 mm (dorsal BLA), -4.56 mm (intermediate BLA), and -4.72 mm (ventral BLA), according to the Mouse Brain in Stereotaxic Coordinates (Franklin and Paxinos 2013)

Tissue sections were washed 3 times, 30 min total, in 0.05M tris-buffered saline solution (TBS pH 7.6). Sections were blocked with TBS containing 10% normal goat serum (NGS) and permeabilized with 0.5% Triton-X100 for 30 min. Sections were then washed with TBS (0.05M pH7.6) for 5 min 3 times. Sections were incubated overnight at room temperature with appropriate primary antibodies (see Table A.3 for the list of antibodies) in 0.5% Triton and 2% NGS. The following day, sections were thoroughly washed with 0.05M TBS 3 times, 10 min per wash. Sections were then incubated for 3 hours, covered from light, with an appropriate secondary antibody conjugated with Alexa Fluor (Table A.3 for details on antibodies and concentrations) in 0.5% Triton and 2% NGS. Sections were washed for 10 minutes 2 times in TBS (0.05M pH 7.6) followed by incubation in Nissl Red staining solution for 20 min. Sections were washed for 5 min 3 times in 0.05M TBS and then 5 min 2 times in 0.05M tris-buffered solution (TB pH7.4), mounted on 0.5% gelatinized slides, and coverslipped with Prolong Diamond Antifade Mountant (Invitrogen, Thermo Fisher). All slides were kept in 4^{o}C until imaging.

B) Retrograde tracing study:

Mice were housed in temperature-controlled cages (with maximum of 5 mice per cage) and maintained on a 12-hour light/dark cycle with *ad libitum* food and water. Stereotaxic injections were conducted on adult wild-type male mice (n=5) aged 8 – 12 weeks (C57BL/6J, Jackson Laboratory). All surgical procedures were performed under aseptic conditions using a stereotaxic instrument (Stoelting, IL). Mice were first anesthetized in an enclosed container with

gaseous isoflurane (5%) and kept under anesthesia (2% isoflurane) using the stereotaxic frame for the entire surgery. Mice were then unilaterally injected to PL (AP: 1.9 mm, ML: -0.4 mm, DV: -2.0 → -1.9 mm) and IL (AP: 2.6 mm, ML: -0.4 mm, DV: -2.8 → -2.7 mm) with Cholera toxin subunit B conjugated with Alexa Fluor 647 or 555 (CtB 647 and CtB 555), respectively (see Table A.3 for details and concentrations). Ten days after injection, animals were perfused as indicated above. 50 µm thick coronal sections were obtained with a Leica vibratome and kept in 0.1M PBS at 4^{o}C for later immunohistochemical processing. Sections containing PL and IL were saved for validation of the injections. Four sections from each animal containing BLA were selected and divided to anterior (AP -1.055mm), intermediate (AP -1.755 mm), posterior (AP -1.855 mm), and super posterior (AP -2.355 mm), approximate Bregma from Allen Mouse Brain Atlas (2004). Sections were subsequently processed for M1R labeling following the procedure above but without Nissl Red staining. All sections from the same animal were processed in the same well and sections from all 3 animals were processed at the same time.

To demonstrate the dense cholinergic innervation from the basal forebrain to the BLA but not CeA, an image of BLA from our anterograde tracing study was also obtained (Figure A.1). Briefly, mice were stereotaxically injected to the basal forebrain with AAV serotype 5 virus expressing GFP under the control of CAG promoter (AAV5-CAG-GFP). Five weeks after injection, 50 µm coronal sections containing BLA were stained with Nissl and imaged (Figure A.1).

C) Image acquisition and data analysis:

All images of PL and IL injection sites were collected using the Invitrogen EVOS FL Auto 2.0 Imaging system (Thermo Fisher Scientific Inc., USA). Ten sections from each animal (n=5, male) containing PL and IL were imaged to verify the specificity and the spread of the injections. Tiled images were acquired at 4X objective using the Texas Red and Cy5 light cubes. The center of each injection as well as its spread was determined with reference to the mouse brain atlas (Franklin and Paxinos 2013). Only mice with the centers of injections contained within PL and IL were selected for further processing and analysis (Figure 2.1, n=3, male).

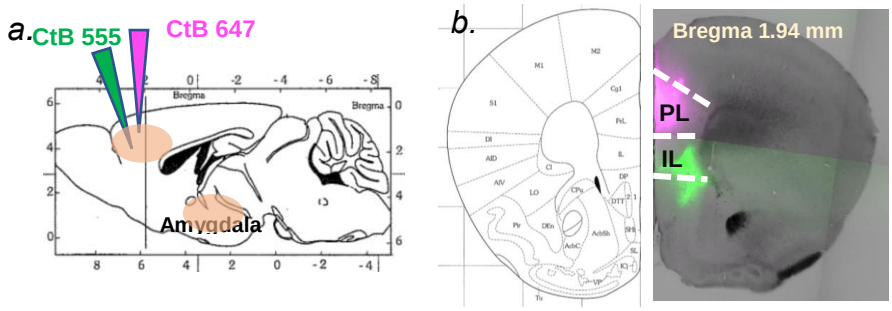

Figure 2.1 Stereotaxic Injection Location and Validation
a: Schematic diagram of injections to PL and IL with CtB 647 (magenta) and CtB 555 (green), respectively. ***b:*** Light microscopic image showing the center of injection at Bregma 1.94 mm with its corresponding atlas image on the left. Atlas images obtained from Paxinos and Franklin (2004).

All sections with BLA were imaged using a Leica SP8 Multiphoton Confocal System (Leica Microsystem Inc., IL, USA). The scope settings for all confocal imaging remained the same throughout vAChT as well as M1 image collection (see Table A.2 for details).

All cell counts and fluorescent intensity measurements were done on Fiji ImageJ 1.52i (National Institutes of Health, USA). The borders between subnuclei were determined on the Nissl channel with reference to the *Franklin and Paxinos' The Mouse Brain in Stereotaxic Coordinates* (Franklin and Paxinos 2013). All images for intensity measurement were converted to 8-bit greyscale. For antero-posterior quantification of vAChT-ir and M1R-ir, evenly spaced, rectangular region-of-interest (ROIs) were generated using the Startup Macros plugins in ImageJ (Figure 2.2a). The *Polygon Selection Tool* was used to outline the BLA. The intersections of the BLA ROI and the rectangular ROIs were generated and added to the *ROI manager* (Figure 2.2b). The average pixel intensity for each of these ROIs were measured and a mouse brain atlas was used to associate the approximate Bregma to the appropriate ROIs (Franklin and Paxinos 2013) (Figure 2.2c).

ROIs of PL- and IL-projectors were outlined using the *Oval Selection Tool* on ImageJ (Figure 2.3). A total of 2,795 projectors were counted (n=3, male). The BLA and its subnuclei were outlined with the *Polygon Selection Tool.* The average pixel intensity of M1R on PL- and IL-projectors were measured using their respective ROIs on the 8-bit greyscale image of the M1R channel (Figure 2.3).

All pixel intensity values were background subtracted before any statistical tests. The average pixel intensity of CeA was set as background. To determine the significant difference between the two means, F-test was first performed to

test the variances of the populations. Student's t-test was then carried out (with either equal or unequal variances according to the results from the F-test).

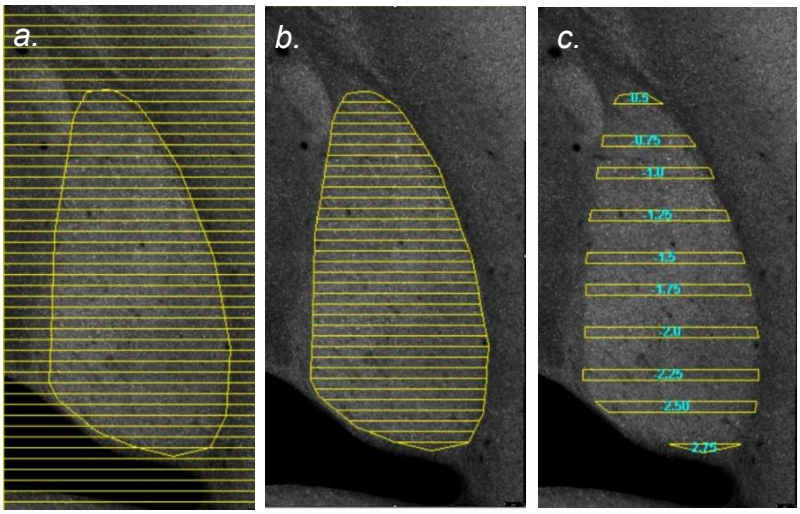

Figure 2.2 ROIs for Antero-posterior Quantification ***a:*** Rectangular ROIs generated with *Startup Macros* plugins in ImageJ and BLA ROI outlined with *Polygon selections Tool.* ***b:*** Intersections of rectangular ROIs and BLA ROIs combined. ***c:*** Selected ROIs with their associated Bregma (numbers in cyan)

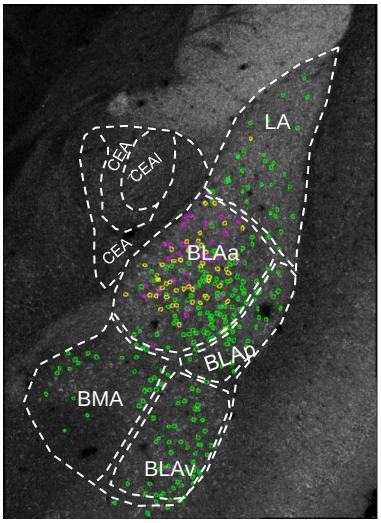

Figure 2.3 ROIs for PL and IL projectors PL-projectors (magenta), IL projectors (green), and dual projectors (yellow)

CHAPTER III: RESULTS

A) Differential Distribution of Cholinergic Innervation:

To elucidate the role of ACh in modulating BLA PNs that are driving antagonistic behaviors, we first examined the differential cholinergic inputs relative to these valence-specific PNs. Not only do these PNs express exclusive genetic markers, they are morphologically distinct with larger-celled magnocellular PNs and smaller-celled parvocellular PNs corresponding to appetitive and aversive behavioral responses, respectively (Kim et al. 2016). Using antibodies to the vesicular acetylcholine transporter (vAChT) to label cholinergic axon terminals, we observed a significant difference in vAChT immunoreactivity (vAChT-ir) surrounding magnocellular versus parvocellular PNs (Figure 3.1 b-d). Specifically, a prominent presence of vAChT+ axons was observed around magnocellular neurons in BLAa whereas a markedly lower density of vAChT+ axons was observed around parvocellular neurons in BLAp (Figures 3.1 and 3.2). No vAChT+ cell bodies were observed in this study. The morphologies of these parvocellular and magnocellular PNs are consistent with those described in an EM study on rat amygdala by McDonald (McDonald 1982). Both cell types show pyramidal-like cell body (Figure 3.2). Quantification on the morphological properties also produced a difference between the soma diameter of these two groups of PNs. Cell bodies of magnocellular PNs are 19-20 µm long and 13-14 µm wide, while cell bodies of parvocellular PNs are 15-16 µm long and

10-11 µm wide (Table A.1). In the transition between BLAa and BLAp, both cell types were found intermingled and surrounded by moderate vAChT labeling (Figure 3.2 g-i).

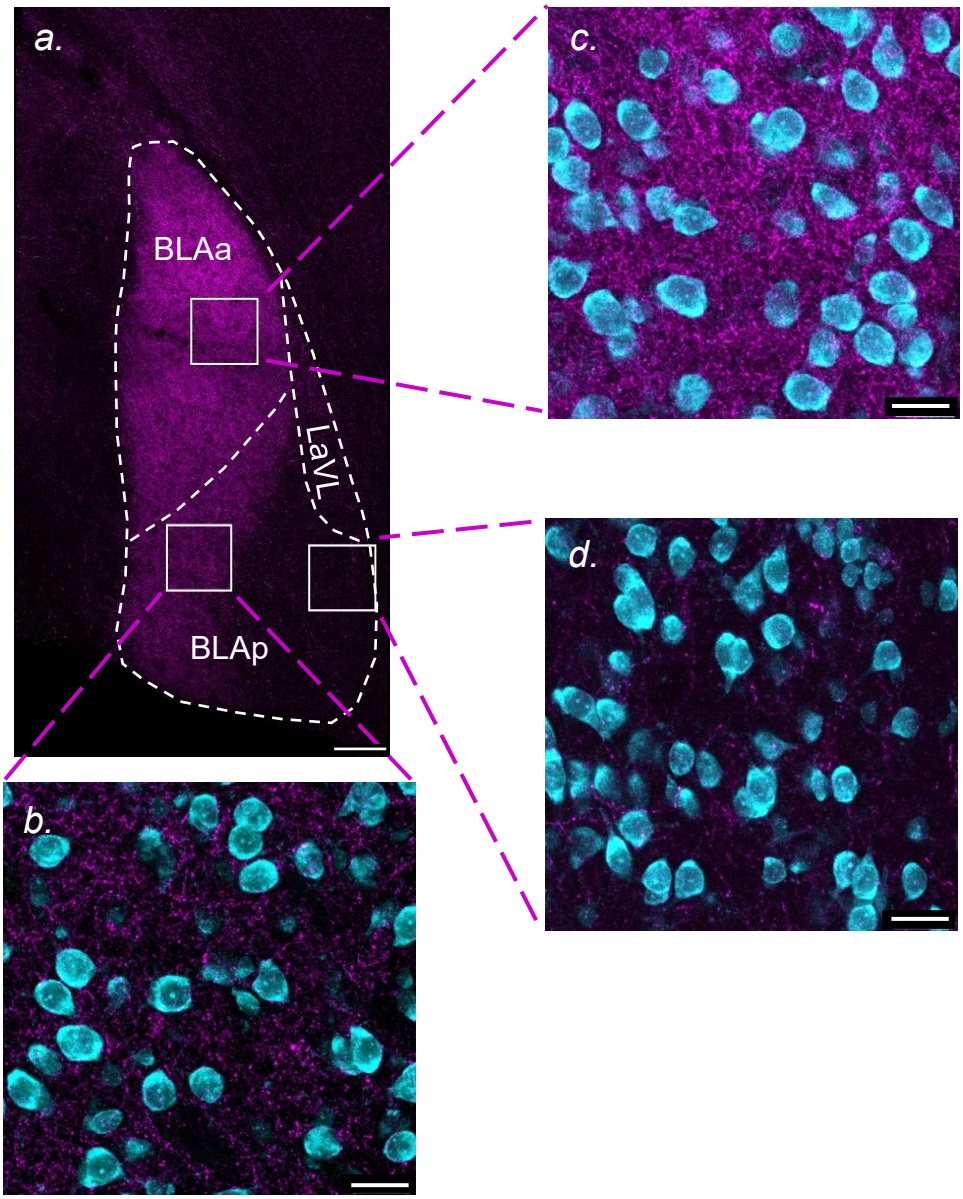

Figure 3.1 vAChT Immunofluorescence. ***a:*** Tiled image of a horizontal BLA showing vAChT-ir (magenta), approximate Bregma -4.56 mm (intermediate section). vAChT density is significantly higher in BLAa compared to that in BLAp and LaVL. ***b, c, d:*** Images of vAChT-ir from BLAa (c), BLAp (d), and at the transition between BLAa and BLAp (b). Cell-body labeled with Nissl stain (cyan). Scale bars: 25 µm (b-d),150 µm (a). z-series: 21.89 µm (a), 5.4 µm (b-d).

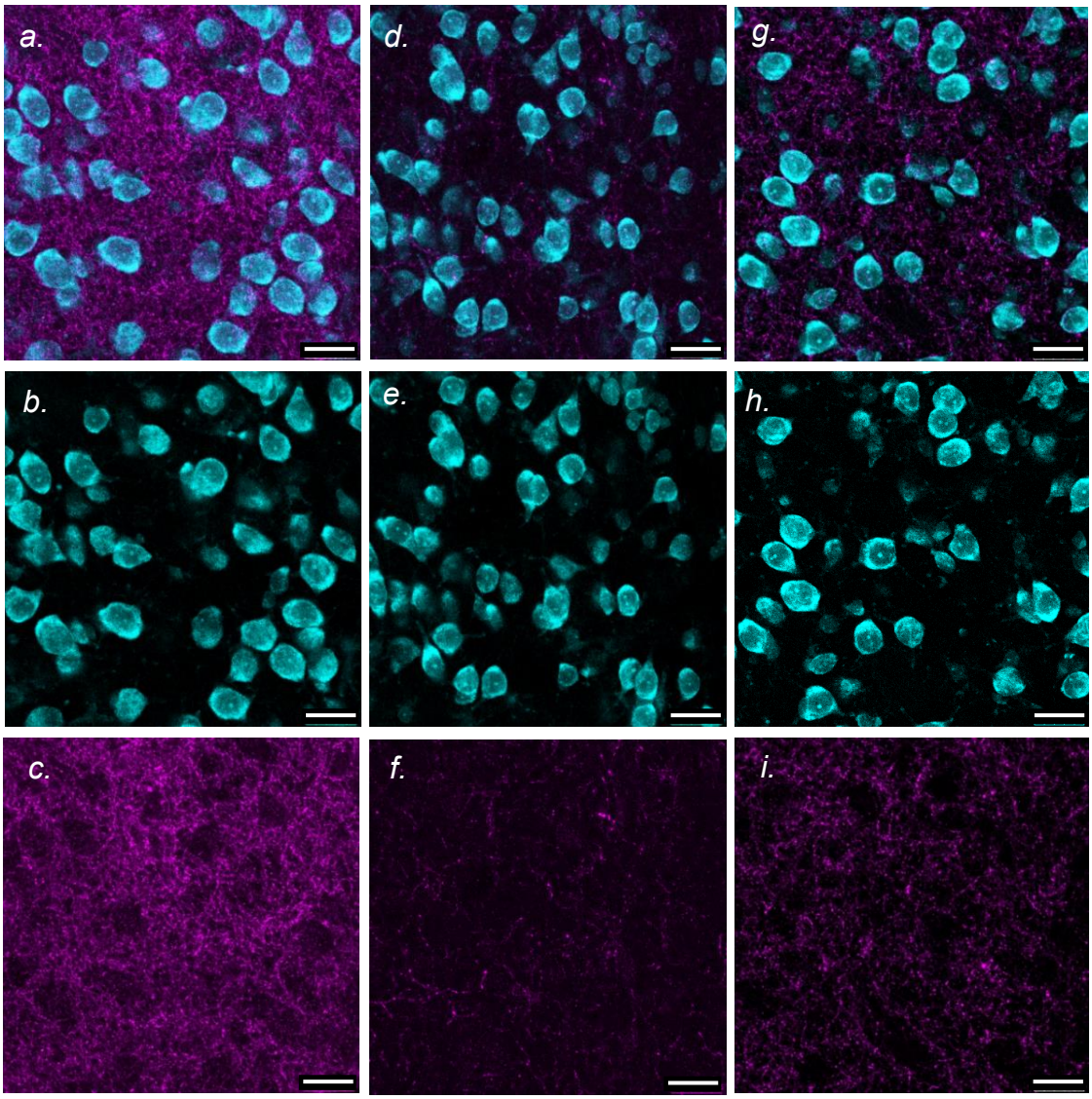

Figure 3.2 vAChT-ir Associated with Parvocellular and Magnocellular PNs. Images showing different density levels of vAChT+ axon terminals in BLAa (a-c), BLAp (d-f), and in the transition between the two subnuclei (g-i). Magnocellular PNs appear with larger cell bodies (b) compared to parvocellular cells (e). A mixture of both cell types can be seen at the transition (h). Scale bars: 25 µm. z-series: 5.4 µm.

A differential distribution of cholinergic inputs between BLA subnuclei was observed using immunoperoxidase technique in a previous report by Muller and colleagues (Muller et al. 2011). Specifically, it was reported that BLAa and BLAp seemed to receive the densest innervation compared to LA, CeA, and BMP.

Based on this assertion, along with our observation on a significant difference in vAChT-ir surrounding PNs in BLAa and BLAp, we quantified and compared the difference in vAChT fluorescent intensity levels along the anterior-to-posterior axis of BLA with approximate Bregma ranged from -0.5 mm to -2.75 mm (Figure 3.3 d-f). This antero-posterior quantification was also examined separately along the DV axis by arbitrarily splitting BLA into 3 groups: dorsal, intermediate, and ventral sections with approximate Bregma of -4.44mm, -4.56 mm, and -4.72 mm, respectively (Figure 3.3) (Franklin and Paxinos 2013). Regarding Muller et al. observation on a low density of vAChT+ axon terminals in central nucleus, we also observed a void of cholinergic fiber in CeA in our anterograde tracing data investigating cholinergic innervation from basal forebrain to different amygdalar subnuclei (Figure A.1). Therefore, we decided to normalize BLA vAChT intensity to CeA vAChT intensity. The intensity of vAChT fluorescent labeling is highest in the anterior region (between Bregma -0.75 mm and -1.25 mm) and substantially decreases moving caudally toward BLAp. This distribution pattern remains consistent throughout the BLA along the DV axis with no apparent sex difference. Almost a 12- to 13-fold difference was measured between the highest intensity around Bregma -1.25 mm and the lowest intensity around Bregma -2.5 mm in the dorsal and intermediate groups (Figure 3.3 a-b). This difference is not as significant in the ventral group (about 3-fold) (Figure 3.3c). Total vAChT-ir levels between BLA subnuclei were also measured and compared (Figure 3.4). As expected, BLAa expressed significantly higher vAChT intensity compared to other subnuclei ($p<0.05$). This is consistent across dorsal, intermediate, and

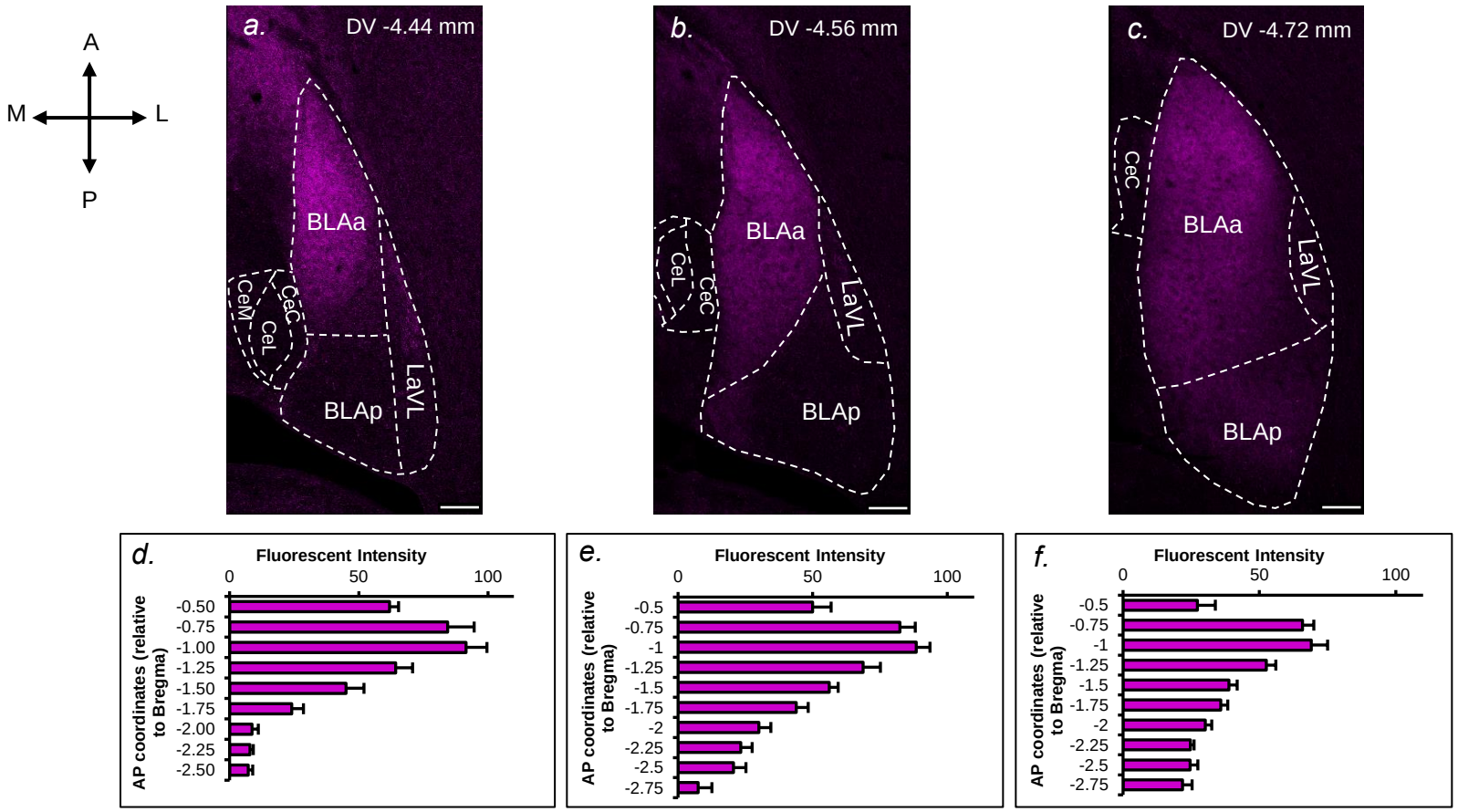

Figure 3.3 Antero-posterior Quantification of vAChT-ir. *a-c*: Representative images of vAChT-ir at dorsal (***a***), intermediate (***b***), and ventral (***c***) levels of BLA (approximate Bregma levels from Paxinos and Franklin 2013. Scale bars 150 µm. ***d-f:*** graphs showing the differential levels of vAChT fluorescent intensity from anterior to posterior BLA at dorsal (d), intermediate (e), and ventral (f) levels. Results show mean ± SEM (n=6, 3 male and 3 female).

ventral BLA with no apparent sex difference (Figure 3.4). Similar to our rostro-caudal quantification above, the difference in this labeling intensity between BLAa and BLAp also reduces in the ventral BLA. Since we only normalized within each group but not between groups, we try to avoid inter-group comparison. However, our observations from the labeling from all 6 animals combined with the values seems to suggest that the overall vAChT fluorescent intensity is higher in dorsal and intermediate BLAa relative to that in ventral BLAp. On the other hand, vAChT-ir in BLAp, although still significantly lower compared to BLAa, seems to increase going from dorsal to ventral BLA. Altogether, our data suggest a preferential bias of cholinergic inputs to magnocellular PNs in BLAa, especially to the dorsal and anterior two-thirds of the BLAa.

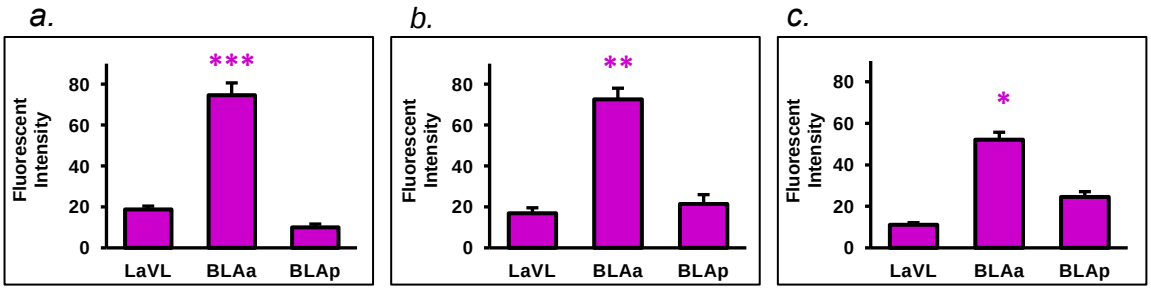

Figure 3.4 Average vAChT Fluorescent Intensity between Different Amygdalar Subnuclei. *a-c*: Bar graphs showing average vAChT fluorescent intensity in BLAa, BLAp and LaVL from dorsal (a), intermediate (b), and ventral (c) BLA. Results show mean ± SEM (n=6, 3 male and 3 female). ***P<0.00001, **P<0.0001, *P<0.0001

B) Differential Distribution of M1 Muscarinic Receptors:

Since a marked difference in the density of vAChT+ axon terminals surrounding magnocellular and parvocellular PNs has been established, we also examined the expression of M1 receptors relative to these populations.

Interestingly, we also observed a difference in the distribution pattern of M1R-ir between these PNs (Figure 3.5 and 3.6). Strong perikaryal staining was observed in the majority of magnocellular PNs. Only a few parvocellular PNs show cell body labeling, all of which were less intense. Perikaryal staining was seen in the cytoplasm but not in the nucleus of PNs which is consistent with previous reports (McDonald and Mascagni 2010). Dense punctate neuropilar staining was observed surrounding both cell types with those surrounding magno- cells appearing to be more dense (Figure 3.6). A 2013 EM study by Muller and colleagues identified neuropilar labeling as mostly from dendritic shafts and spines, as well as many axon terminals (Muller et al. 2013). Somata diameters between these two population were also quantified and displayed consistent results with previous reports (Table A.1)

Following the establishment of a spatial bias of cholinergic inputs to different amygdalar subnuclei, we examined the distribution pattern of M1R between these subnuclei. McDonald and Mascagni previously reported, in an immunohistochemistry study on rat, a variation in immunoreactivity levels of M1 receptors between different nuclei of the amygdala with the most robust labeling in the anterior two-thirds of the BLA (McDonald and Mascagni 2010). Based on this assertion, together with our observation above on the differential levels of M1R-ir between magno- and parvo- cells, we performed similar antero-posterior quantification as in our vAChT study. Similar distribution patterns across dorsal, intermediate, and ventral regions of BLA were observed (Figure 3.7).

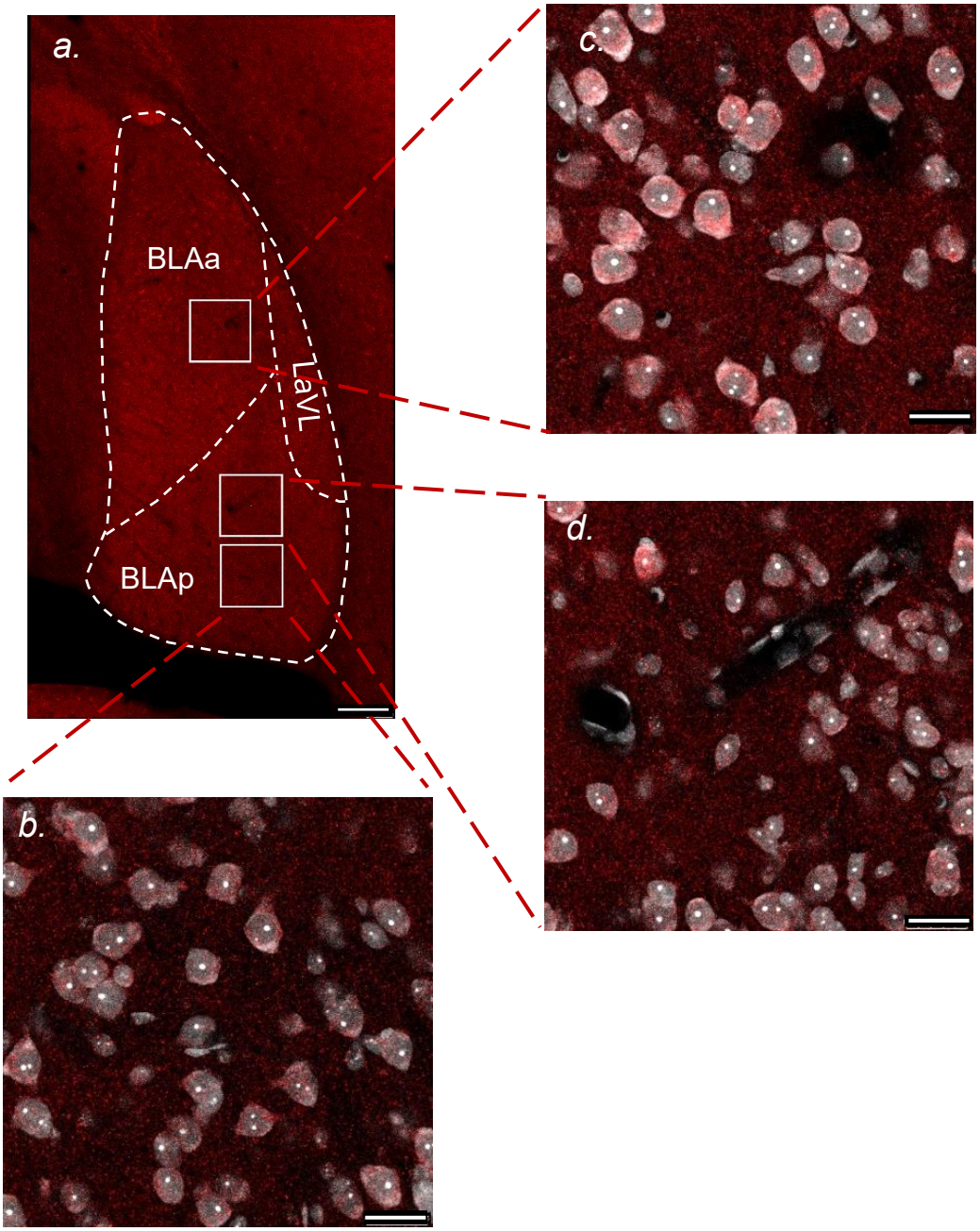

Figure 3.5 M1R Immunofluorescence. ***a:*** Tiled image of a horizontal BLA sho M1R-ir (red) at Bregma level -4.56 mm (intermediate section). ***b, c, d:*** Images of M1R-ir from BLAa (c) and BLAp (b,d). Strong perikaryal labeling in magnocellular PNs in BLAa (c). Cell body labeled with Nissl stain (grey). Scale bars: 25 µm (b-d), 150 µm (a). z-series: 21.89 µm (a), 4.97 µm (b-d).

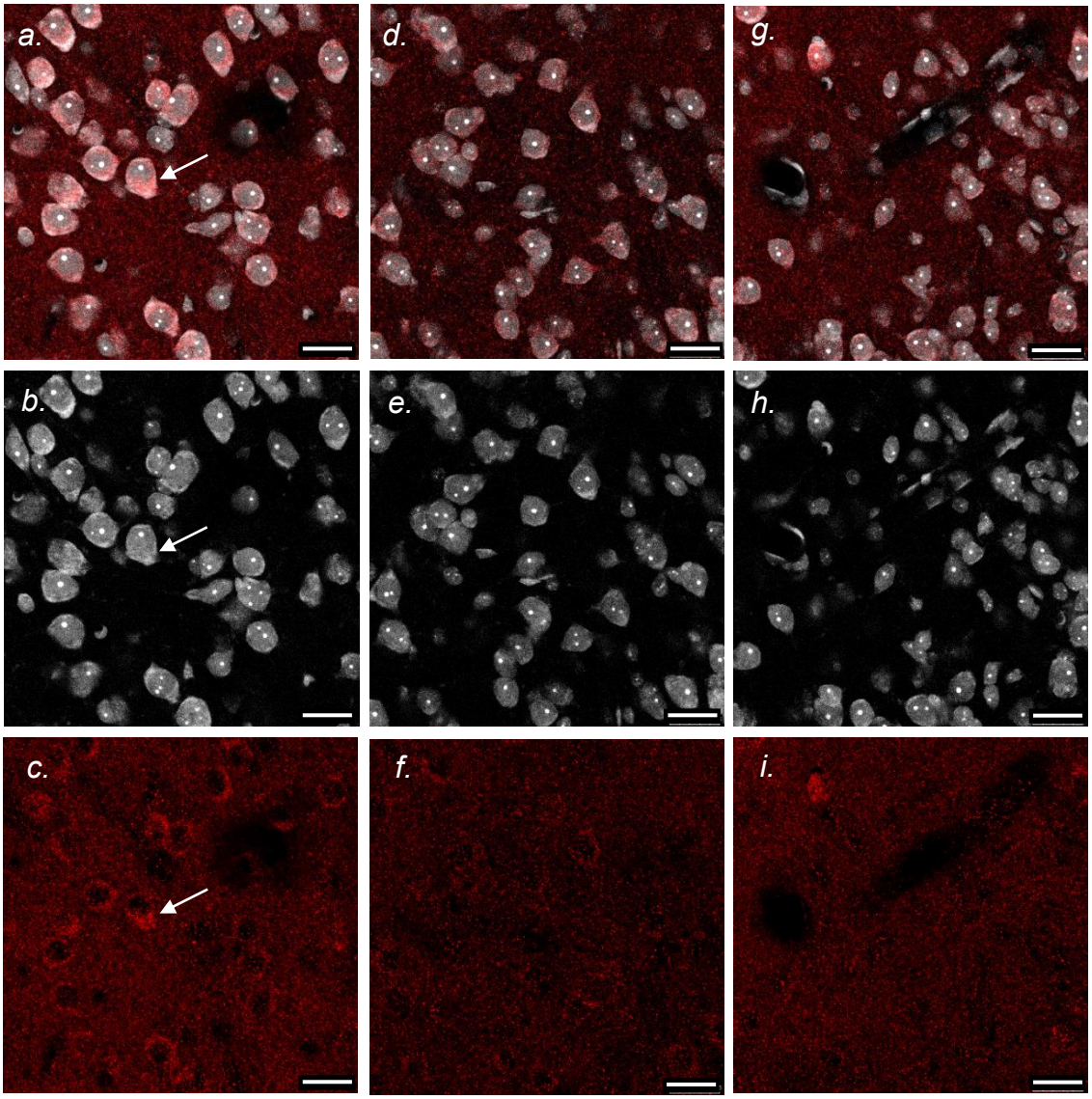

Figure 3.6 M1R-ir Relative to Parvocellular and Magnocellular PNs. ***a:*** Images depict differential expression of M1R in BLAa (a-c), BLap (d-i). Morphologies of magnocellular (b) and parvocellular (e, h) PNs are consistent with those observed from our vAChT study. Strong perikaryal staining can be observed in the cytoplasm and proximal dendrites of magnocellular PNs (c). Very light soma labeling can be observed in a few parvocellular PNs (f). The neuropilar labeling surrounding magnocellular PNs (c) seems to be more dense than that surrounding parvocellular PNs (f, i). Scale bars: 25 µm. z-series: 5.4 µm

Consistently, the highest intensity was measured approximately around Bregma -1.50 mm to -1.75 mm. M1R-ir intensity seems to remain consistently high moving rostrally from Bregma -1.75 mm up to -1.00 mm in intermediate and ventral regions, but a 30% drop was measured in the dorsal sections. The most rostral region (Bregma -0.5 to -0.75 mm) expressed the lowest level of M1. Overall, the caudal two-thirds of BLAa seem to express the highest M1R intensity followed by the rostral part of BLAa and BLAp, both of which seem to express M1R-ir equally. Interestingly, this AP distribution of M1R, especially from male animals, resembles the AP distribution of nociceptive neurons in BLA previously reported by Corder et al. (2019) (Figure 3.7 and 3.8). We observed a slight different pattern in female mice which is more of a bell shape. Average M1R-ir in BLA subnuclei were also determined. Along the DV axis, the highest average M1R intensity was measured in BLAa and the lowest was measured in BLAp. However, the intensity difference between BLAa and BLAp was only significant in the dorsal sections (Figure 3.9).

C) Differential Expression of M1R between PL- and IL- Projectors:

It was suggested that PNs in BLAa and BLAp project to PL and IL, respectively (Kim et al. 2016). Since we have seen a significant difference in M1R expression between these BLA subnuclei, a similar pattern of expression should be observed between PL and IL projectors in BLA. We first determined the topographical distribution of PL- and IL- projectors along the AP axis of BLA. A total of 2,795 CtB+ projectors were counted from 3 male mice, which is approximately 932 cells per animal. On average, 838 IL projectors and 297 PL

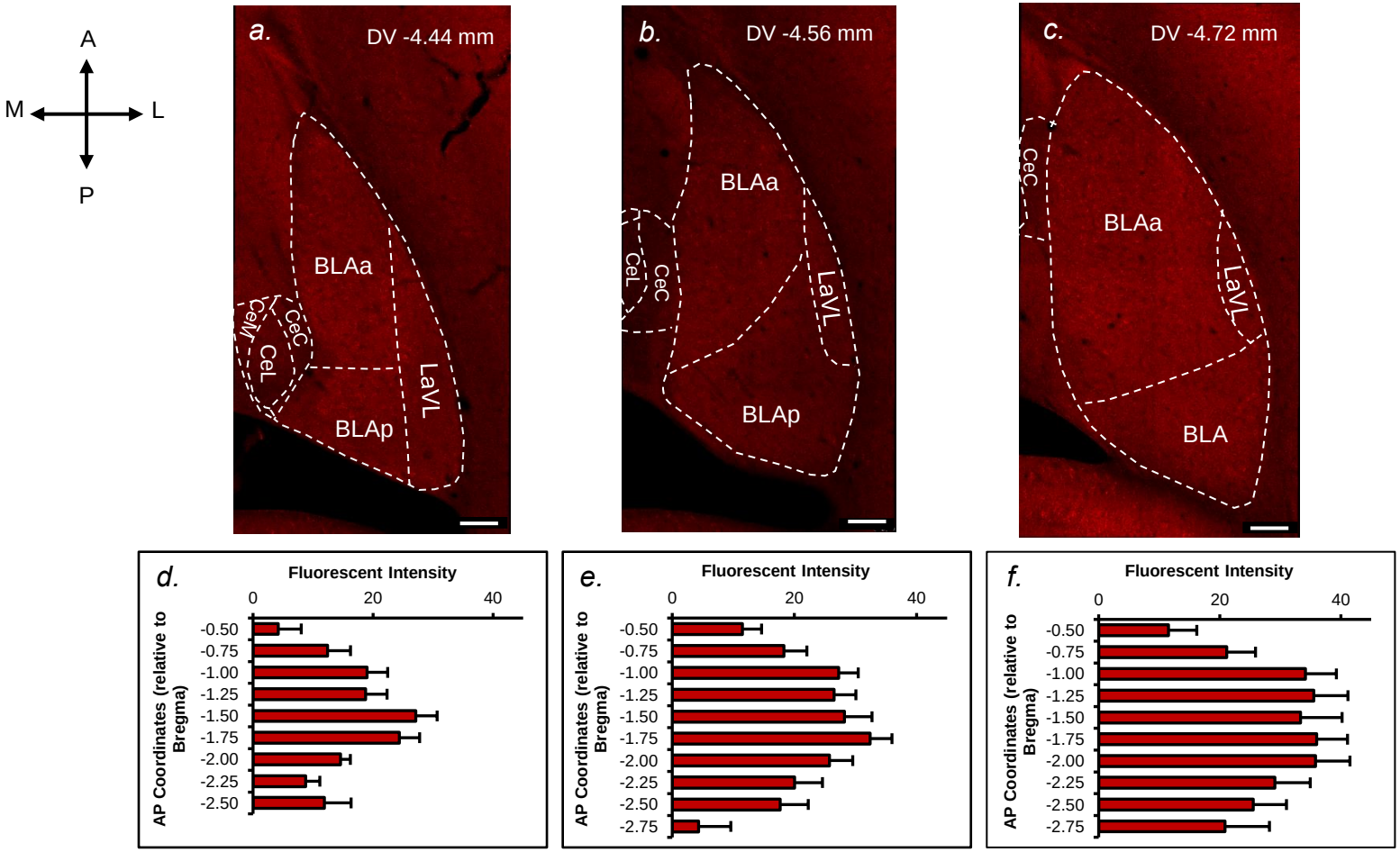

Figure 3.7 Antero-posterior Quantification of M1R-ir. *a-c*: Representative images of M1R-ir at dorsal (***a***), intermediate (***b***), and ventral (***c***) levels of BLA (approximate Bregma levels from Paxinos and Franklin 2013). Scale bars 150 µm. ***d-f:*** graphs showing the differential levels of M1R fluorescent intensity from anterior to posterior BLA at dorsal (d), intermediate (e), and ventral (f) levels. Results show mean ± SEM (n=6, 3 male and 3 female).

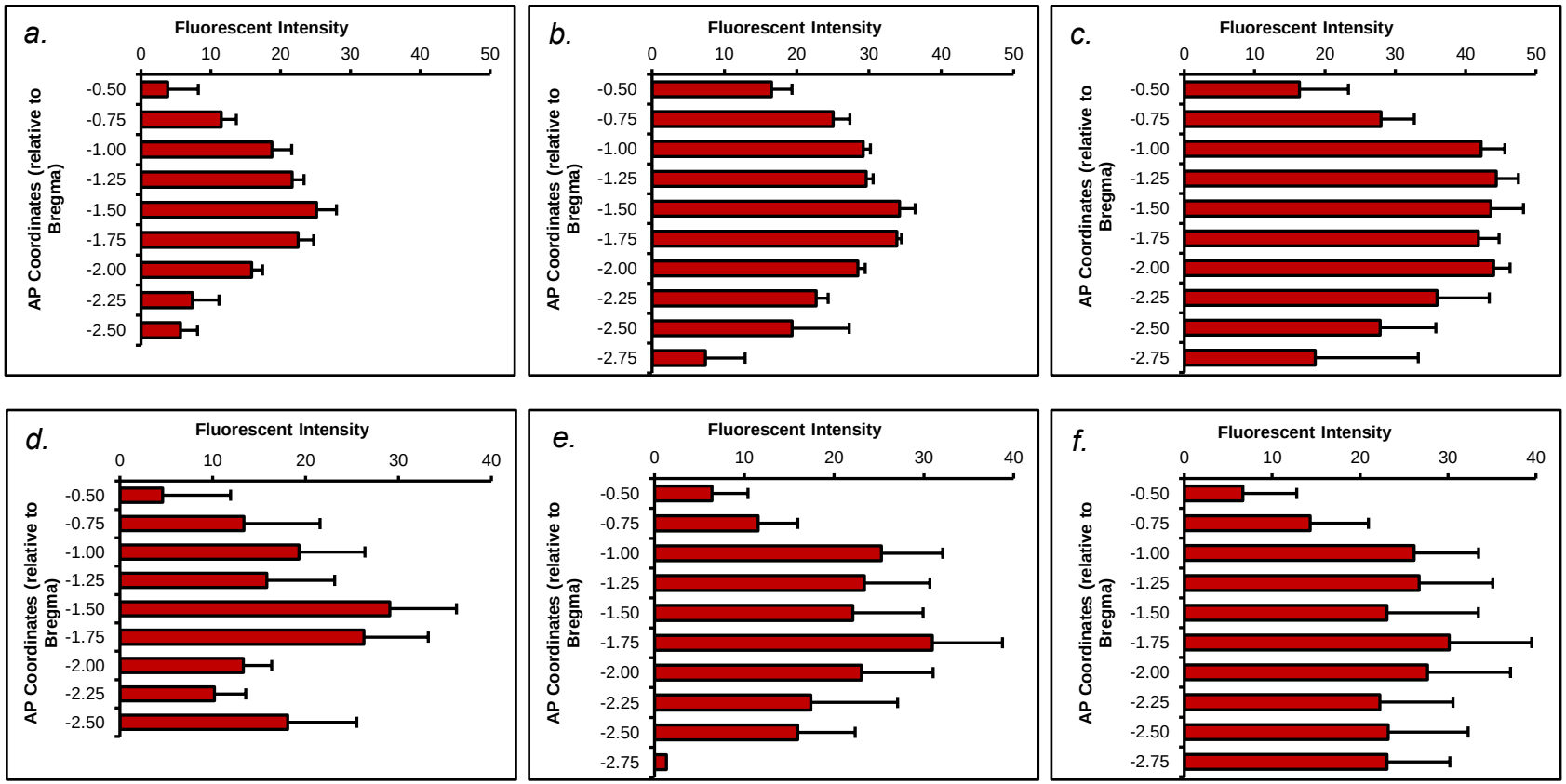

Figure 3.8 Male versus Female Difference in Antero-posterior Distribution of M1R-ir. The difference in the distribution patterns of M1R fluorescent intensity along the AP axis (Bregma -0.5 to -2.75 mm) from female (a-c) versus male (d-f). Results show mean ± SEM (a-c: n=3, female; d-f: n=3, male)

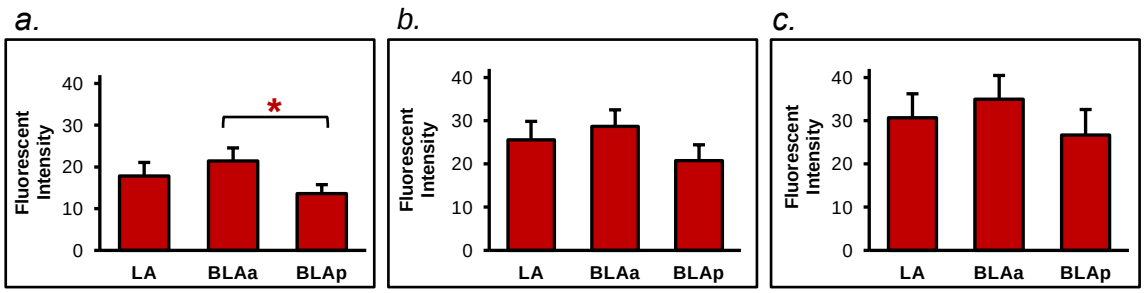

Figure 3.9 Average M1R Fluorescent Intensity between BLA Subnuclei. **a-c:** Bar graphs showing average M1R fluorescent intensity in LA, BLAa, and BLAp from dorsal (a), intermediate (b), and ventral (c) BLA. Intensity measured in BLAa is significantly higher than that in BLAp in dorsal sections. Results show mean ± SEM (n=6, 3 male and 3 female). *P<0.05

projectors were recorded with 203 of those (68.5% of PL-projectors and 24.5% of IL-projectors) beign dual projectors that project to both IL and PL. From this point, IL- and PL- projectors referred to those that solely project to IL or PL and not including dual projectors. Topographically, most of the PL projecting neurons clustered in the anterior region of BLA (Bregma -1.055 mm to -1.755 mm), while IL projecting neurons dispersed throughout, spanning from the lateral part of intermediate BLA to the posterior portion of BLA (Bregma -1.755mm to -2.355 mm) (Figures 3.10 a-d, A.3). This distribution was quantified along the AP axis, regardless of BLA subnuclei. 53% of PL projectors (49 out of 93 cells) were found in the intermediate BLA (Bregma -1.755 mm), which contains a major portion of BLAa. Only 8% of PL-projectors were found in the posterior region of BLA (Bregma -2.255 to -2.355 mm), which consists of a small caudal part of BLAa and a large portion of BLAp. The remaining PL-projectors were equally distributed between anterior and posterior regions (~20% each). IL-projectors were evenly distributed (20-30% each) to intermediate, posterior, and super-posterior BLA. We then determined the soma labeling of M1R on PL- and IL-

projectors along this AP distribution (Figure 3.10 g). Since we disregard the subnuclei, it seems that both projector populations express a similar level of M1R-ir while PL-projectors express a slightly higher intensity than IL-projectors throughout. Both projector populations expressed the highest intensity in the rostral BLA (Bregma -1.255 mm) and the lowest intensity in the most caudal region (Bregma -2.255 mm) with a 3- to 4- fold difference.

We also looked at the distribution of PL- and IL-projectors between BLA subnuclei (Figure 3.11). The majority of PL-projectors (69%) were located in BLAa. IL-projectors, however, did not project any topographical bias between subnuclei. Interestingly, when we measured the M1R-ir intensity of each projector population and compared them between subnuclei, substantial differences were observed. Overall, both PL- and IL- projectors in LA and BLAa expressed significantly higher M1R intensity than those in BLAp, BMAp, and BLAv ($p<0.001$). We also looked at the AP segregation of PL- and IL-projectors within BLAa and BLAp (Figure 3.12). Within BLAa, 75% of PL-projectors were found between Bregma -1.255 and -1.755 mm, where the brightest M1R intensity were measured. When we measured the M1R intensity between PL- and IL-projectors within the same subnuclei (either BLAa or BLAp), no significant difference was detected. However, significant differences were measured when we compared them between subnuclei, even within the same projector population (Figure 3.13 b). Overall, the average M1R intensity in PL projectors is significantly higher than M1R intensity in IL projectors.

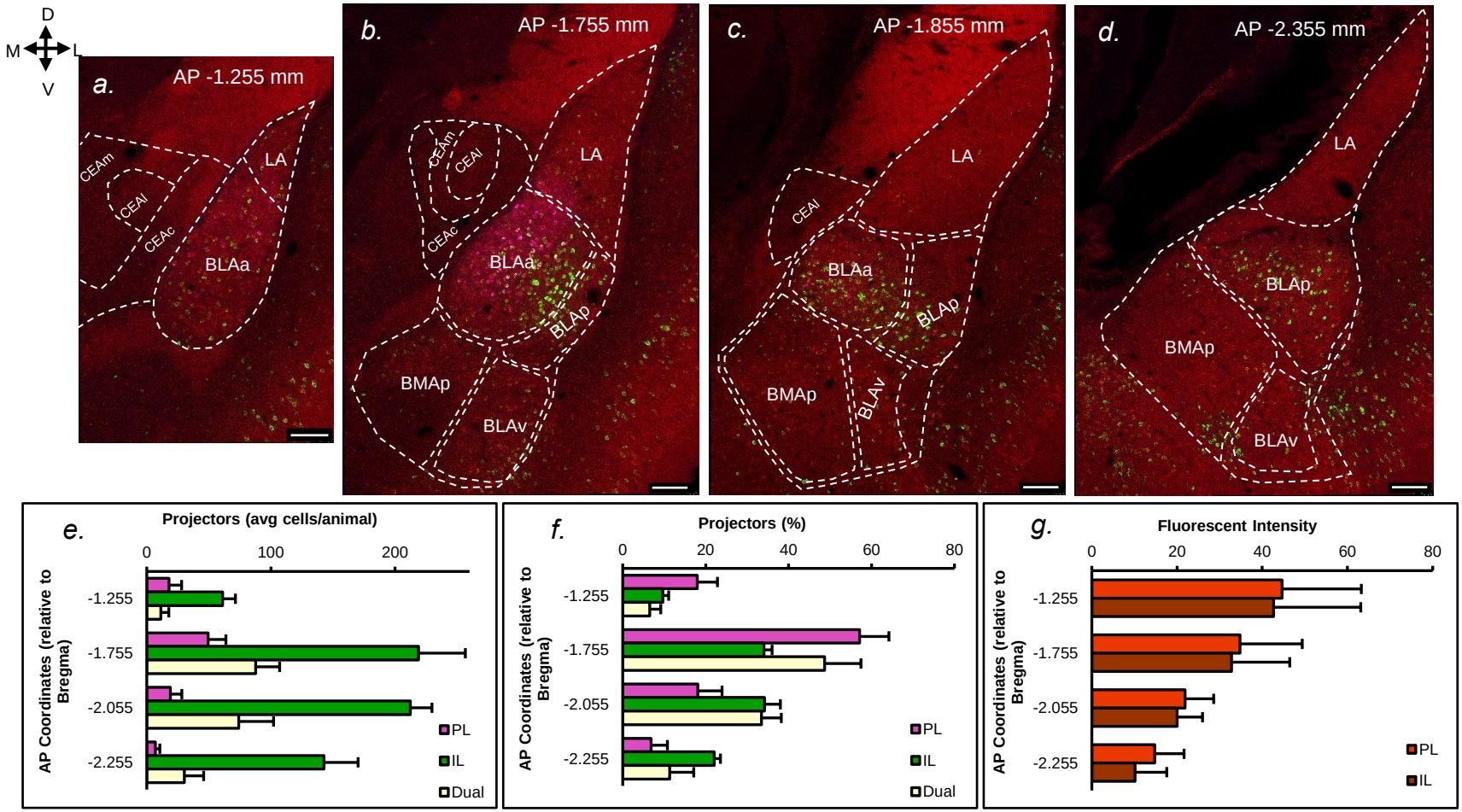

Figure 3.10 Antero-posterior Distribution of PL- and IL- projectors and of their Perikaryal M1R Labeling. ***a-d:*** Images of coronal sections of BLA at anterior (a), intermediate (b), posterior (c), and super-posterior levels (d). Images showing M1R-ir (red), PL projectors (magenta), and IL projectors (green). Scale bars: 150 µm. ***e,f:*** AP distribution of PL- and IL- projectors (regardless of subnuclei). ***g:*** M1R intensity on PL- and IL- projectors along the AP axis. Results show mean ± SEM (n=3, male).

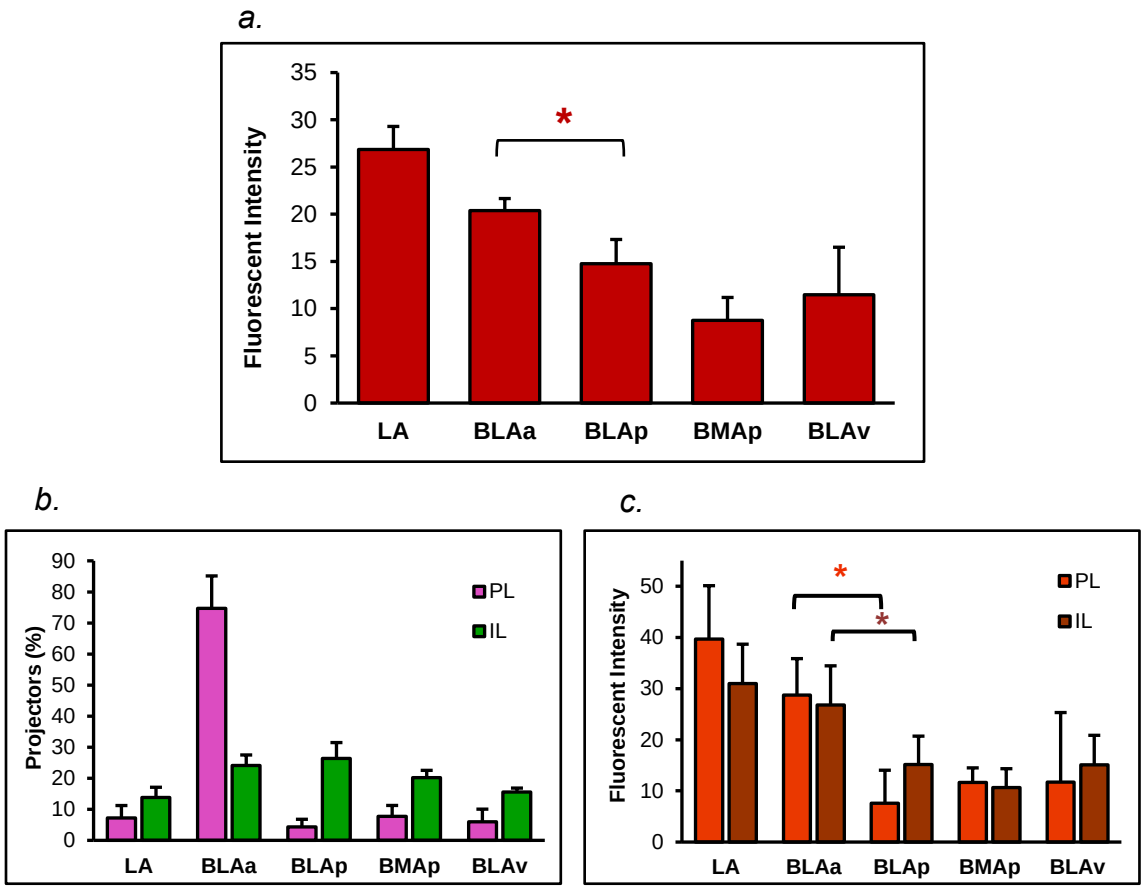

Figure 3.11 Distribution of PL- and IL-projectors and their Relative M1R-ir between BLA subnuclei. ***a:*** Average M1R fluorescent intensity between BLA subnuclei. M1R intensity in BLAa is significantly higher than that in BLAp ($p<0.05$). ***b:*** Distribution of PL-and IL- projectors (%) in different subnuclei. ***c:*** M1R intensity of PL- and IL- projectors in different subnuclei. PL- and IL-projectors in BLAa express significantly higher levels of M1R-ir fluorescent intensity than those in BLAp ($p<0.001$). Results show mean ± SEM (n=3, male).

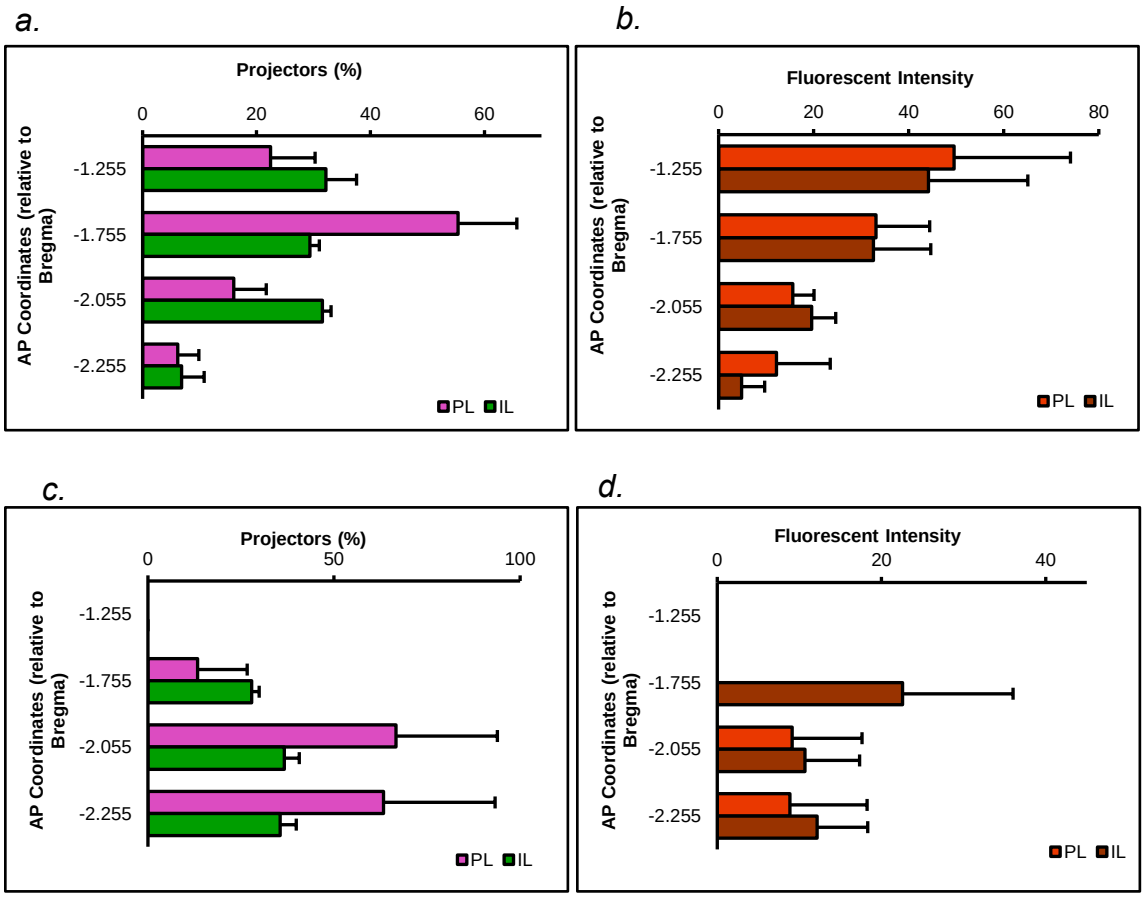

Figure 3.12 AP Distribution of PL- and IL-projectors in BLAa and BLAp and their M1R-ir. ***a,c:*** AP distribution of PL- and IL-projectors (%) within BLAa (a) and BLAp (c). ***b,d:*** Average M1R fluorescent intensity of PL- and IL-projectors with their approximate location along the AP axis within BLAa (b) and BLAp (d). Results show mean ± SEM (n=3, male)

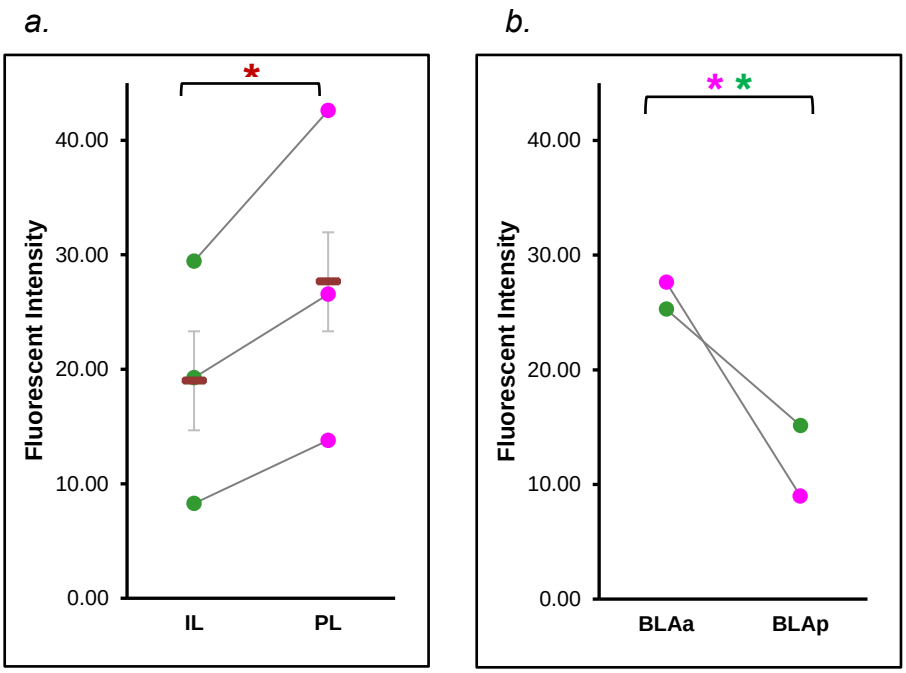

Figure 3.13 Differential Expression of M1R between PL- and IL- Projectors and between Subnuclei. ***a:*** Differential expression of M1R between PL and IL projectors (magenta and green, respectively (*p<0.001). ***b:*** Differential expression of M1R between PL-projectors in BLAa and those in BLAp (magenta, *p<0.001)); as well as between IL-projectors in BLAa and those in BLAp (green, *p<0.01). Results show mean ± SEM (n=3, male).

CHAPTER IV: DISCUSSION

A previous EM study by Muller and colleagues reported that dendritic shafts and spines of PNs in BLAa are the main targets of cholinergic inputs from the basal forebrain (Muller et al. 2011). Physiological properties of BLA PNs are also altered by cholinergic transmission. Together, these studies suggested that PNs' functions in BLAa are largely modulated by cholinergic signaling. Valence-specific PNs in BLA are not only spatially segregated, but they also express distinct morphological properties and genetic markers. We wanted to determine whether these distinct BLA PNs differentially express cholinergic markers. Topographically, we have established a differential distribution of cholinergic innervation between BLA subnuclei as well as between these two groups of PNs. Specifically, magnocellular PNs are surrounded by dense cholinergic terminals, whereas parvocellular PNs receive significantly less innervation. The moderate labeling captured at the transition between BLAa and BLAp, where a mixture of both cell types was observed, seems to further implicate magnocellular PNs as the main target of cholinergic inputs. Since magnocellular and parvocellular PNs define the architecture of BLA to BLAa and BLAp, we also quantified the labeling intensity of different BLA subnuclei. A substantial difference in vAChT labeling intensity between BLAa and BLAp was measured. Unlike the observation by Muller et al. (2011) from their light microscopic result about a dense vAChT-ir in BLAp, we observed a very light labeling in BLAp, which is not much different from

that in the ventrolateral LA (LaVL). This could be due to species differences or the difference in sensitivity and specificity between antibodies and enzymes employed by immunofluorescence versus immunoperoxidase techniques. Interestingly, there seems to be a spatial segregation within BLAa and BLAp subnuclei. Specifically, the rostral and dorsal two-thirds of BLAa seems to express brighter vAChT intensity than its caudoventral counterpart. However, the higher intensity observed in the ventral portion of BLAp compared to its dorsal region could be due to it being transitioned to BMAp. Since BMAp is the parvocellular subdivision of BMA, it is difficult to discern from the parvocellular cells in BLAp. Together, our data suggest magnocellular PNs that drive negative valences receives significantly higher levels of cholinergic inputs compared to parvocellular PNs that drive positive valences.

As mentioned above, dendritic shafts and spines of PNs are the main targets of cholinergic inputs to BLAa (Muller et al. 2011). The same group also reported in their 2013 EM study that almost all dendritic shafts (90%), 60% of dendritic spines, and many axon terminals in the BLAa were M1R+. Collectively, these studies suggest a crucial role of M1R to the cholinergic effects onto PNs. Similar to our vAChT study, we also examined the distribution of M1R across BLA subnuclei and between parvocellular and magnocellular PNs. We found a high portion of magnocellular cells in BLAa showing strong perikaryal staining, specifically in the cell cytoplasm and proximal dendrite. The same EM study also confirmed that these perikaryal M1R were associated with the endoplasmic reticulum and Golgi apparatus, indicating that they are in the process of being

transported to distal dendrites and spines. Interestingly, we could not observe such strong staining in the soma of parvocellular PNs. One possibility is that parvocellular PNs are more efficient at transporting proteins to their processes. If that is the case, we should observe a higher neuropilar labeling in BLAp than that in BLAa. However, it seems that neuropilar staining in BLAa is still relatively more dense. Further analysis investigating the difference in neuropilar labeling as well as the proportion of different M1R+ neuropilar structures between BLAa and BLAp is needed.

We also quantified the fluorescent intensity of M1R along the AP axis and between subnuclei. Opposite to our vAChT results, we found the ventrocaudal portion of BLAa expressed the brightest M1R intensity. Our finding on the marked resemblance between the AP distribution of M1R and the distribution of nociceptive neurons (reported by Corder et al., 2019) suggests that M1R may be preferentially expressed on a subset of negative neurons. It would be interesting to see if this distribution pattern persists when we quantify perikaryal M1R-ir after injection of colchicine, a substance that blocks the transportation of proteins from a cell body to its processes. The higher M1R-ir intensity measured in the ventral portion of BLAp, again, could be due to the transition between BLAp and BMAp. Also, neuropilar structures from PNs in neighboring subnuclei such as BMAp or BLAv could also contribute to this increase in intensity.

When we measured the M1R-ir fluorescence intensity between different projector populations in BLA, we were able to show that the differential expression of M1R between these PNs correlates to their topographical

distribution. Specifically, PL projectors, whose AP distribution matched that of M1R, expressed significantly higher M1R than IL projectors, which were more evenly distributed. Another study in our lab looking at other projector populations found similar results. Particularly, we found that CeM projectors, whose presence is significantly higher in BLAp than BLAa (~5-fold difference), expressed significantly lower M1R intensity than NAc projectors, whose distribution between BLAa and BLAp is less skewed. Previous reports have shown that the downstream projection target defines the specific valence of BLA PNs (Namburi et al. 2015; Beyeler et al. 2016; Beyeler et al. 2018). However, studies on the neural basis of this valence segregation suggested that this projection-based idea is not sufficient (Kim et al. 2016). Particularly, although the first group reported that NAc projectors in BLA are driven by positive stimuli, the latter group pointed out that this could be due to a higher percentage of NAc projectors being ppp1r1b+. It would be interesting to compare the expression of M1R between Ppp1r1b+ and Rspo2+ NAc projectors. We were able to show that magnocellular IL projectors in BLAa expressed significantly higher M1R expression than parvocellular IL projectors in BLAp. This implicates that M1Rs are differentially expressed on Rspo2+ and Ppp1r1b+ IL projectors. Future studies using specific antibodies for Ppp1r1b and Rspo2 are suggested.

Several studies indicated that PNs in the BLA drive antagonistic behavioral responses. Our data suggested a differential expression of cholinergic markers between these opposing valence-encoding PNs in the BLA. Specifically, we established a preferential bias of cholinergic inputs and receptors to

magnocellular PNs in BLAa that correspond to negative valences. Electrophysiological studies have shown that cholinergic inputs from the basal forebrain (BF) result in biphasic responses in PNs of BLA. Specifically, photo-stimulation of cholinergic terminals originated from BF induced a large inhibitory response followed by a slower, sustained M1R-mediated excitatory response in BLA PNs (Aitta-aho et al. 2018). Interestingly, another study reported that the effects of BF inputs on BLA PNs depend on their active state (Unal et al. 2015). Specifically, BF cholinergic signaling excites active PNs and inhibits inactive PNs in BLA, which can enhance the signal-to-noise ratio. The inhibitory effect exerted by BF inputs on PNs at rest occurred through two phases. The first phase was through a nicotinic-mediated activation of local GABAergic neurons, which subsequently inhibit PNs. The second phase was via a direct activation of M1Rs on PNs. The excitatory effect induced by BF inputs on active PNs was also suggested to be M1R-mediated (Unal et al. 2015). The significant presence of cholinergic markers in BLAa compared to their weak labeling in BLAp in our study suggest that this signal-to-noise enhancement mechanism regulated by ACh is more prevalent in negative PNs. It is possible that PL- and IL- projectors residing in BLAa which are responsive to negative stimuli receive a more precise modulatory mechanism by cholinergic signaling than their counterparts in BLAp which are responsive to positive stimuli.

REFERENCES

Aitta-aho T, Hay YA, Phillips BU, Saksida LM, Bussey TJ, Paulsen O, Apergis-Schoute J. 2018. Basal Forebrain and Brainstem Cholinergic Neurons Differentially Impact Amygdala Circuits and Learning-Related Behavior. Current Biology. 28(16):2557-2569.e4. doi:10.1016/j.cub.2018.06.064.

Bartus RT, Dean RL, Beer B, Lippa AS. 1982. The cholinergic hypothesis of geriatric memory dysfunction. Science. 217(4558):408–414.

Bartus RT, Johnson HR. 1976. Short-term memory in the rhesus monkey: Disruption from the anti-cholinergic scopolamine. Pharmacology Biochemistry and Behavior. 5(1):39–46. doi:10.1016/0091-3057(76)90286-0.

Bechara A. 2001. Neurobiology of decision-making: risk and reward. Semin Clin Neuropsychiatry. 6(3):205–216.

Bechara A, Damasio AR, Damasio H, Anderson SW. 1994. Insensitivity to future consequences following damage to human prefrontal cortex. Cognition. 50(1–3):7–15.

Bechara A, Damasio H. 2002. Decision-making and addiction (part I): impaired activation of somatic states in substance dependent individuals when pondering decisions with negative future consequences. Neuropsychologia. 40(10):1675–1689.

Bechara A, Damasio H, Damasio AR. 2003. Role of the amygdala in decision-making. Ann N Y Acad Sci. 985:356–369.

Bechara A, Damasio H, Damasio AR, Lee GP. 1999. Different contributions of the human amygdala and ventromedial prefrontal cortex to decision-making. J Neurosci. 19(13):5473–5481.

Bechara A, Tranel D, Damasio H. 2000. Characterization of the decision-making deficit of patients with ventromedial prefrontal cortex lesions. Brain. 123 (Pt 11):2189–2202.

Beyeler A, Chang C-J, Silvestre M, Lévêque C, Namburi P, Wildes CP, Tye KM. 2018. Organization of Valence-Encoding and Projection-Defined Neurons in the Basolateral Amygdala. Cell Reports. 22(4):905–918. doi:10.1016/j.celrep.2017.12.097.

Beyeler A, Namburi P, Glober GF, Simonnet C, Calhoon GG, Conyers GF, Luck R, Wildes CP, Tye KM. 2016. Divergent Routing of Positive and Negative Information from the Amygdala during Memory Retrieval. Neuron. 90(2):348–361. doi:10.1016/j.neuron.2016.03.004.

Braak H, Braak E, Yilmazer D, de Vos RAI, Jansen ENH, Bohl J. 1996. Pattern of brain destruction in Parkinson's and Alzheimer's diseases. Journal of Neural Transmission. 103(4):455–490. doi:10.1007/BF01276421.

Braak H, Braak E, Yilmazer D, de Vos RAI, Jansen ENH, Bohl J, Jellinger K. 1994. Amygdala pathology in Parkinson's disease. Acta Neuropathologica. 88(6):493–500. doi:10.1007/BF00296485.

Buckley N, Bonner T, Brann M. 1988. Localization of a family of muscarinic receptor mRNAs in rat brain. The Journal of Neuroscience. 8(12):4646–4652. doi:10.1523/JNEUROSCI.08-12-04646.1988.

Corder G, Ahanonu B, Grewe BF, Wang D, Schnitzer MJ, Scherrer G. 2019. An amygdalar neural ensemble that encodes the unpleasantness of pain. Science. 363(6424):276–281. doi:10.1126/science.aap8586.

Correia SS, Goosens KA. 2016. Input-specific contributions to valence processing in the amygdala. Learn Mem. 23(10):534–543. doi:10.1101/lm.037887.114.

Crook JM, Tomaskovic-Crook E, Copolov DL, Dean B. 2000. Decreased muscarinic receptor binding in subjects with schizophrenia: a study of the human hippocampal formation. Biol Psychiatry. 48(5):381–388.

Dean B, McLeod M, Keriakous D, McKenzie J, Scarr E. 2002. Decreased muscarinic1 receptors in the dorsolateral prefrontal cortex of subjects with schizophrenia. Mol Psychiatry. 7(10):1083–1091. doi:10.1038/sj.mp.4001199.

Franklin KBJ, Paxinos G. 2013. Paxinos and Franklin’s The mouse brain in stereotaxic coordinates. Fourth edition. Amsterdam: Academic Press, an imprint of Elsevier.

Gold PE. 2003. Acetylcholine modulation of neural systems involved in learning and memory. Neurobiol Learn Mem. 80(3):194–210.

Gupta R, Koscik TR, Bechara A, Tranel D. 2011. The amygdala and decision making. Neuropsychologia. 49(4):760–766. doi:10.1016/j.neuropsychologia.2010.09.029.

Harding AJ, Stimson E, Henderson JM, Halliday GM. 2002. Clinical correlates of selective pathology in the amygdala of patients with Parkinson's disease. Brain. 125(11):2431–2445. doi:10.1093/brain/awf251.

James W. 1884. What is an Emotion? Mind. 9(34):188–205.

Kan Y, Kawamura M, Hasegawa Y, Mochizuki S, Nakamura K. 2002. Recognition Of Emotion From Facial, Prosodic And Written Verbal Stimuli In Parkinson'S Disease. Cortex. 38(4):623–630. doi:10.1016/S0010-9452(08)70026-1.

Kandel E. 2018. The Disordered Mind. First. [accessed 2019 Mar 12]. https://us.macmillan.com/books/9780374287863.

Kawai H, Lazar R, Metherate R. 2007. Nicotinic control of axon excitability regulates thalamocortical transmission. Nature Neuroscience. 10(9):1168–1175. doi:10.1038/nn1956.

Kiehl KA, Hoffman MB. 2011. THE CRIMINAL PSYCHOPATH: HISTORY, NEUROSCIENCE, TREATMENT, AND ECONOMICS. Jurimetrics. 51:355–397.

Kim J, Pignatelli M, Xu S, Itohara S, Tonegawa S. 2016. Antagonistic negative and positive neurons of the basolateral amygdala. Nature Neuroscience. 19(12):1636–1646. doi:10.1038/nn.4414.

Kobayakawa M, Koyama S, Mimura M, Kawamura M. 2008. Decision making in Parkinson's disease: Analysis of behavioral and physiological patterns in the Iowa gambling task. Movement Disorders. 23(4):547–552. doi:10.1002/mds.21865.

Kobayakawa M, Tsuruya N, Kawamura M. 2010. Sensitivity to reward and punishment in Parkinson's disease: An analysis of behavioral patterns using a modified version of the Iowa gambling task. Parkinsonism & Related Disorders. 16(7):453–457. doi:10.1016/j.parkreldis.2010.04.011.

Krettek JE, Price JL. 1978. A description of the amygdaloid complex in the rat and cat with observations on intra-amygdaloid axonal connections. Journal of Comparative Neurology. 178(2):255–279. doi:10.1002/cne.901780205.

LeDoux J. 2003. The Emotional Brain, Fear, and the Amygdala. Cellular and Molecular Neurobiology.:12.

Lein ES, Hawrylycz MJ, Ao N, Ayres M, Bensinger A, Bernard A, Boe AF, Boguski MS, Brockway KS, Byrnes EJ, et al. 2007. Genome-wide atlas of gene expression in the adult mouse brain. Nature. 445(7124):168–176. doi:10.1038/nature05453.

Levey A, Kitt C, Simonds W, Price D, Brann M. 1991. Identification and localization of muscarinic acetylcholine receptor proteins in brain with subtype-specific antibodies. The Journal of Neuroscience. 11(10):3218–3226. doi:10.1523/JNEUROSCI.11-10-03218.1991.

Mascagni F, McDonald AJ, Coleman JR. 1993. Corticoamygdaloid and corticocortical projections of the rat temporal cortex: APhaseolus vulgaris leucoagglutinin study. Neuroscience. 57(3):697–715. doi:10.1016/0306-4522(93)90016-9.

McDonald A, Mascagni F. 2010. Neuronal localization of m1 muscarinic receptor immunoreactivity in the rat basolateral amygdala. Brain Structure and Function. 215(1):37–48. doi:10.1007/s00429-010-0272-y.

McDonald AJ. 1982. Neurons of the lateral and basolateral amygdaloid nuclei: A golgi study in the rat. The Journal of Comparative Neurology. 212(3):293–312. doi:10.1002/cne.902120307.

McDonald AJ. 1998. Cortical pathways to the mammalian amygdala. Progress in Neurobiology. 55(3):257–332. doi:10.1016/S0301-0082(98)00003-3.

McGaugh JL. 2004. The amygdala modulates the consolidation of memories of emotionally arousing experiences. Annu Rev Neurosci. 27:1–28. doi:10.1146/annurev.neuro.27.070203.144157.

McGeer PL, McGeer EG, Suzuki J, Dolman CE, Nagai T. 1984. Aging, Alzheimer’s disease, and the cholinergic system of the basal forebrain. Neurology. 34(6):741–745.

Muller JF, Mascagni F, McDonald AJ. 2011. Cholinergic Innervation of Pyramidal Cells and Parvalbumin-Immunoreactive Interneurons in the Rat Basolateral Amygdala. J Comp Neurol. 519(4):790–805. doi:10.1002/cne.22550.

Muller JF, Mascagni F, Zaric V, McDonald AJ. 2013. Muscarinic cholinergic receptor M1 in the rat basolateral amygdala: Ultrastructural localization and synaptic relationships to cholinergic axons: M1R in the Basolateral Amygdala. Journal of Comparative Neurology. 521(8):1743–1759. doi:10.1002/cne.23254.

Namburi P, Beyeler A, Yorozu S, Calhoon GG, Halbert SA, Wichmann R, Holden SS, Mertens KL, Anahtar M, Felix-Ortiz AC, et al. 2015. A circuit mechanism for differentiating positive and negative associations. Nature. 520(7549):675–678. doi:10.1038/nature14366.

Picciotto MR, Higley MJ, Mineur YS. 2012. Acetylcholine as a Neuromodulator: Cholinergic Signaling Shapes Nervous System Function and Behavior. Neuron. 76(1):116–129. doi:10.1016/j.neuron.2012.08.036.

Power AE, McIntyre CK, Litmanovich A, McGaugh JL. 2003. Cholinergic modulation of memory in the basolateral amygdala involves activation of both m1 and m2 receptors. Behav Pharmacol. 14(3):207–213. doi:10.1097/01.fbp.0000073702.15098.21.

Rice ME, Cragg SJ. 2004. Nicotine amplifies reward-related dopamine signals in striatum. Nature Neuroscience. 7(6):583–584. doi:10.1038/nn1244.

Robinson L, Platt B, Riedel G. 2011. Involvement of the cholinergic system in conditioning and perceptual memory. Behav Brain Res. 221(2):443–465. doi:10.1016/j.bbr.2011.01.055.

Romanski LM, LeDoux JE. 1993. Information Cascade from Primary Auditory Cortex to the Amygdala: Corticocortical and Corticoamygdaloid

Projections of Temporal Cortex in the Rat. Cerebral Cortex. 3(6):515–532. doi:10.1093/cercor/3.6.515.

Sah P, Faber ESL, Lopez De Armentia M, Power J. 2003. The Amygdaloid Complex: Anatomy and Physiology. Physiological Reviews. 83(3):803–834. doi:10.1152/physrev.00002.2003.

Saito Y, Kawashima A, Ruberu NN, Fujiwara H, Koyama S, Sawabe M, Arai T, Nagura H, Yamanouchi H, Hasegawa M, et al. 2003. Accumulation of Phosphorylated α-Synuclein in Aging Human Brain. Journal of Neuropathology & Experimental Neurology. 62(6):644–654. doi:10.1093/jnen/62.6.644.

Scarr E, Sundram S, Keriakous D, Dean B. 2007. Altered hippocampal muscarinic M4, but not M1, receptor expression from subjects with schizophrenia. Biol Psychiatry. 61(10):1161–1170. doi:10.1016/j.biopsych.2006.08.050.

Schwartz B. The Paradox of Choice. [accessed 2019 Mar 19]. https://www.goodreads.com/work/best_book/1157840-the-paradox-of-choice-why-more-is-less.

Sprengelmeyer R, Young AW, Mahn K, Schroeder U, Woitalla D, Büttner T, Kuhn W, Przuntek H. 2003. Facial expression recognition in people with medicated and unmedicated Parkinson’s disease. Neuropsychologia. 41(8):1047–1057. doi:10.1016/S0028-3932(02)00295-6.

Suzuki A, Hoshino T, Shigemasu K, Kawamura M. 2006. Disgust-specific impairment of facial expression recognition in Parkinson's disease. Brain. 129(3):707–717. doi:10.1093/brain/awl011.

Treffers T, Fehse K. 2016. The Neural Correlates of Emotion and Overconfidence in Strategic Decision Making. In: Decision Making in Behavioral Strategy. Charlotte, NC: Information Age Publishing. p. 83–98. [accessed 2019 Mar 18]. http://eds.b.ebscohost.com.pallas2.tcl.sc.edu/ehost/ebookviewer/ebook/bmxlYmtfXzE0MjQyNzFfX0FO0?sid=954bbeec-3bbb-4faf-9d52-c1f60064e315@pdc-v-sessmgr02&vid=0&format=EB&rid=1.

Unal CT, Pare D, Zaborszky L. 2015. Impact of Basal Forebrain Cholinergic Inputs on Basolateral Amygdala Neurons. Journal of Neuroscience. 35(2):853–863. doi:10.1523/JNEUROSCI.2706-14.2015.

Whitehouse PJ, Price DL, Struble RG, Clark AW, Coyle JT, Delon MR. 1982. Alzheimer's disease and senile dementia: loss of neurons in the basal forebrain. Science. 215(4537):1237–1239.

Wonnacott S. 1997. Presynaptic nicotinic ACh receptors. Trends in Neurosciences. 20(2):92–98. doi:10.1016/S0166-2236(96)10073-4.

Yechiam E, Hayden EP, Bodkins M, O'Donnell BF, Hetrick WP. 2008. Decision making in bipolar disorder: A cognitive modeling approach. Psychiatry Research. 161(2):142–152. doi:10.1016/j.psychres.2007.07.001.

Zhang H, Sulzer D. 2004. Frequency-dependent modulation of dopamine release by nicotine. Nature Neuroscience. 7(6):581–582. doi:10.1038/nn1243.

APPENDIX A: SUPPLEMENTARY DATA AND FIGURES

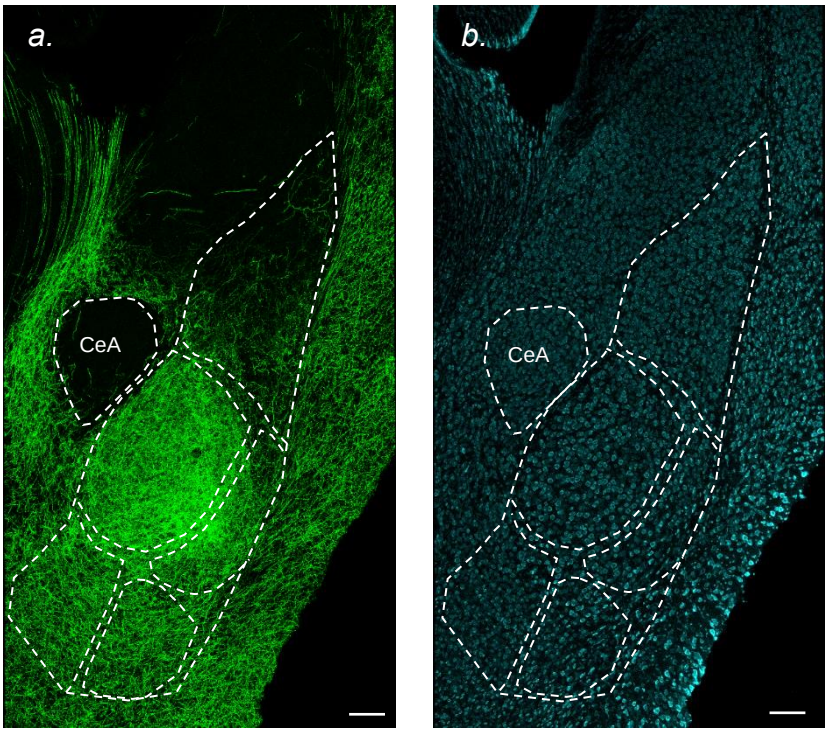

Figure A.1 Innervation of Cholinergic Fibers from the Basal Forebrain in BLA. Cholinergic fibers (green, a) termination in BLA. No fibers were observed in CeA. Cell bodies labeled with Nissl stain (cyan, b). Scale bars: 150 µm

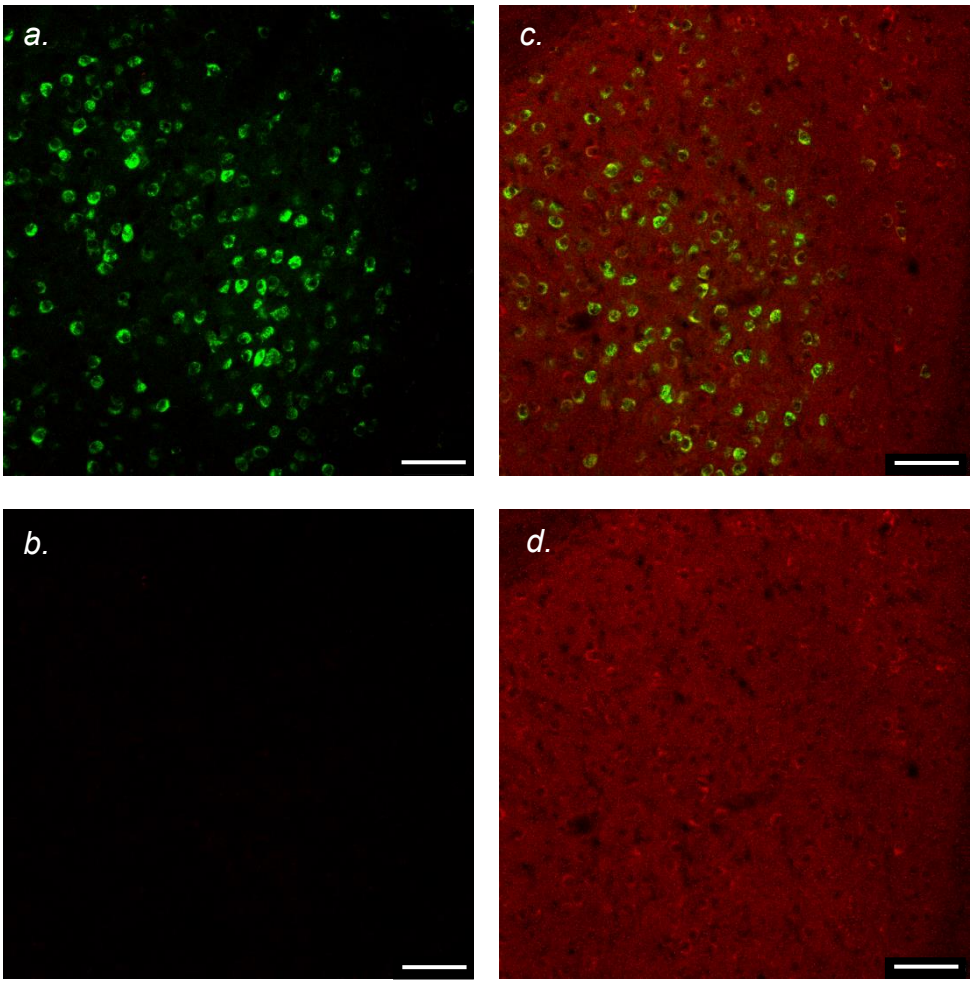

Figure A.2 Antibody Specificity. Images of BLAa showing NAc projectors (green) and M1R (red) with α-M1R antibody (c,d) and without α-M1R antibody (a,b). Scale bars: 75 µm

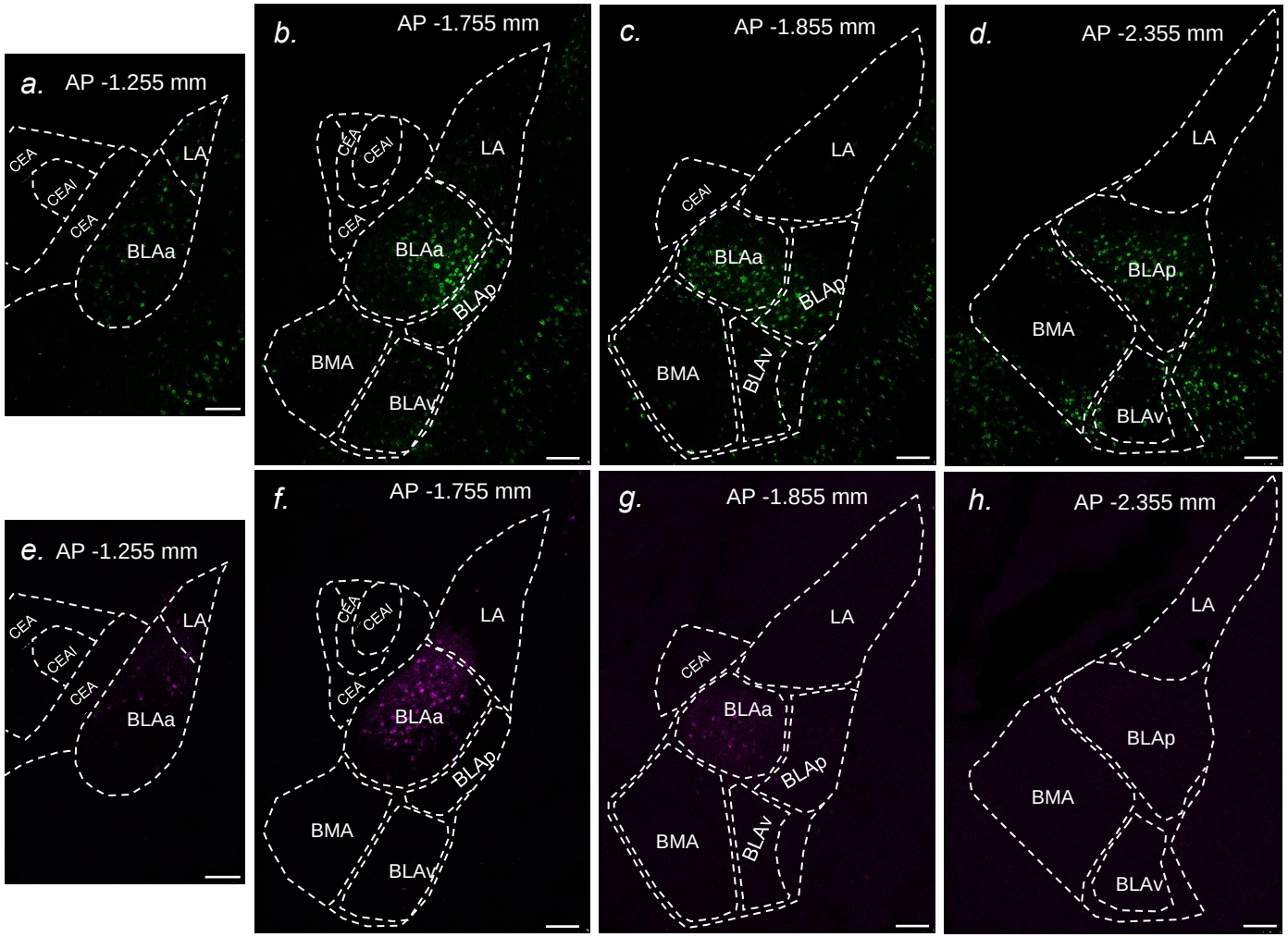

Figure A.3 PL- and IL-projectors Distribution Images of coronal sections showing the distribution of IL projectors (a-d) and PL projectors (e-h) from anterior (a,e), intermediate (b,f), posterior (c,g), and super-posterior (d,h) BLA. Scale bars: 150 µm. z-series: 21.89 µm

Table A.1 Soma diameters of magnocellular and parvocellular PNs.

	Soma Diameter (µm)	
Cell Type	**Length**	**Width**
Magnocellular (n=17)	19.54 ± 0.35	13.42 ± 0.34
Parvocellular (n=16)	15.40 ± 0.17	10.98 ± 0.20

Table A.2 Microscope setting for Leica SP8.

	Pinhole	Laser line - Intensity	Gain	Scan speed	x (µm)	y (µm)	z (µm)
63X - vAChT	2 AU - 200.6 um	552 nm - 0.2503%	100	400 Hz	175.74	175.74	5.4
		638 nm - 1.3%					
63X - M1	1.5 AU -	488 nm - 1.3%	100	400 Hz	175.74	175.74	4.97
		552 nm - 0.55%					
20X	1 AU - 59.5 um	488 nm - 1.3%	100	400 Hz	553.57	553.57	21.89
		552 nm - 0.35%	100				
		638 nm - 0.85%	100				

Table A.3 Antibodies and other products details.

	Target	Antibody	Company	Concentration	Product number
1° Ab	M1R	Rabbit anti-mAChR-M1-Rb-Af340	Frontier Institute Co., ltd	1:400	AB_2571791
	vAChT	goat anti-Vesicular Acetylcholine Transporter	Millipore	1:1,500	ABN100
2° Ab	Rabbit	Goat anti-rabbit-Alexa Fluor 488	Thermo Fisher	1:400	A21447
	Goat	Donkey anti-goat-Alexa Fluor 647	Thermo Fisher	1:400	A-11008
	Nissl substance	NeuroTrace™ 530/615 Red Fluorescent Nissl Stain	Invitrogen	1:100	N21482
Retrograde Tracer		Cholera toxin B , Alexa Fluor™ 555 conjugate (CtB 555)	Invitrogen	0.15 µL (injection volume)	C34776
		Cholera toxin B, Alexa Fluor™ 647 conjugate (CtB 647)	Invitrogen	0.15 µL (injection volume)	C34778